

MASSIVE STAR FORMING REGIONS IN THE GALAXY USING THE SPITZER GLIMPSE SURVEY

MUBDI RAHMAN¹ AND NORMAN MURRAY^{2,3}*Draft version April 21, 2010*

ABSTRACT

We examine the thirteen most luminous sources in the WMAP free-free map using the Spitzer GLIMPSE and MSX surveys to identify massive star formation regions, emitting one-third of the Galactic free-free luminosity. We identify star forming regions by a combination of bubble morphology in 8 μ m (PAH) emission and radio recombination line radial velocities. We find 40 star forming regions associated with our WMAP sources, and determine unique distances to 31. We interpret the bubbles as evidence for radial expansion. The radial velocity distribution for each source allows us to measure the intrinsic speed of a region's expansion. This speed is consistent with the size and age of the bubbles. The high free-free luminosities, combined with negligible synchrotron emission, demonstrate that the bubbles are not driven by supernovae. The kinetic energy of the largest bubbles is a substantial fraction of that measured in the older superbubbles found by Heiles. We find that the energy injected into the ISM by our bubbles is similar to that required to maintain the turbulent motion in the gas disk inside 8 kpc. We report a number of new star forming regions powered by massive ($M_* > 10^4 M_\odot$) star clusters. We measure the scale height of the Galactic O stars to be $h_* = 35 \pm 5$ pc. We determine an empirical relationship between the PAH and free-free emission of the form $F_{\text{PAH}} \propto F_{\text{ff}}^2$. Finally, we find that the bubble geometry is more consistent with a spherical shell rather than a flattened disk.

Subject headings: infrared: ISM – ISM: H II regions – stars: formation

1. INTRODUCTION

Massive star forming regions provide a unique laboratory to study both the process of massive star formation and feedback within the Galaxy. These clusters are home to the most massive stars in the Galaxy, including the vast majority of O and B stars. The stars in turn produce most of the ionizing luminosity and stellar winds that inject energy and momentum into the interstellar medium (ISM), blowing bubbles and producing shell structures. Finally, the most massive stars explode as supernovae, which also inject energy and momentum into the ISM.

The most massive star clusters ($M_* > 10^4 M_\odot$), referred to as *super star clusters*, have been regularly observed in extragalactic star forming regions (Ho 1997), but until recently such massive clusters have evaded detection in our own Galaxy. This has largely been due to the heavy dust obscuration within our own Galactic disk. Over the last decade a number of young, massive clusters have been found in the Galaxy, including the Arches and Quintuplet clusters near the Galactic centre region (Figer et al. 1999), Westerlund 1 (Clark et al. 2005), and RSGC 1, 2, & 3 (Figer et al. 2006; Davies et al. 2007; Clark et al. 2009), either by directly imaging the stars, or by the stellar radio emission.

Another possible method of locating these young, massive star forming regions is to look for the environmen-

tal effects caused by such clusters, such as H II regions, or shell and bubble structures. These effects can be observed in wavebands where extinction through the Galactic plane becomes less of an issue, such as the radio and infrared. Extensive surveys of H II regions both in the northern and southern sky have been conducted with limited success in finding these massive star forming regions (for a recent census, refer to Conti & Crowther 2004).

In Murray & Rahman (2010, hereafter Paper I), we used the Wilkinson Microwave Anisotropy Probe (WMAP) maximum entropy method free-free foreground emission map (Bennett et al. 2003a; Gold et al. 2009) to determine the star formation rate in the Galaxy. We found that the 18 most luminous regions (located within 13 WMAP sources) produce over half the total ionizing luminosity of the Galaxy, implying that half the total number of O stars reside in these regions. These sources contain bubble structures having radii ranging from 5 to 100 pc. Most of the ionizing photons from the embedded stellar population escape the bubble and ionize the surrounding material, creating the Extended Low-Density regions (ELD) (Lockman 1976; Anantharamaiah 1985a,b). Examination of the Spitzer Galactic Legacy Infrared Midplane Survey Extraordinaire (GLIMPSE) 8 μ m images shows that many known H II regions appear on shells or walls of bubbles. These known H II regions are generated either by the illumination of swept up material by the central cluster, or by star formation triggered in the swept up material. In either case, the luminosity of the central cluster is larger than that given by summing the total emission from all of the H II regions in the area.

Further, a large number of the known H II regions in a WMAP source had not previously been associated with one another, a result of their disparate radial velocities.

rahman@astro.utoronto.ca

¹ Department of Astronomy & Astrophysics, University of Toronto, 50 St. George Street, Toronto, Ontario, M5S 3H4, Canada² Canadian Institute for Theoretical Astrophysics, University of Toronto, 60 St. George Street, Toronto, Ontario, M5S 3H8, Canada³ Canada Research Chair in Astrophysics

The range of radial velocities had been translated into different distances along the line of sight. We, on the other hand, interpret the differences in radial velocity as the result of bubble expansion; the H II regions lie on shells, with velocity differences of order 15 km s^{-1} , consistent with the expected expansion speed of a bubble in the ISM, e.g., Harper-Clark & Murray (2009).

In this paper we analyze the most luminous WMAP sources using the GLIMPSE and MSX surveys, and previously known H II region velocities. We describe our procedure for associating the H II and PAH emission using an intrinsic expansion velocity criteria in §2. We discuss the general properties of the star forming regions (which we define in §2.1) in §3. We discuss each of the star forming regions in depth in Section 4. In Section 5, we determine the scale height of O stars in the Galactic disk, quantify the relationship between the PAH and free-free emission, discuss the expansion of the star forming regions as a turbulent driving mechanism of the Galaxy’s molecular gas, and comment on the three-dimensional geometry of observed bubble structures. Finally, we summarize our results in Section 6.

2. DATA ANALYSIS

In Paper I, we divided the total flux of the WMAP regions along a given line of sight based on various distance determinations (radio recombination lines, molecular absorption lines, and stellar distances). Using this division, one-third of the Galactic free-free emission arises from 14 discrete WMAP sources. These sources contain more than one-third of the O star population of the Galaxy.

Here we investigate in more detail, using additional radial velocities, the 13 most luminous free-free sources in the Galaxy from Paper I (we exclude the Galactic Centre region since it is so well studied already).

Each of the WMAP sources are fit by ellipses, with major axes between ~ 2 to 5 degrees; sizes, positions and fluxes are given in Table 1. These sources are confused (contain multiple star forming regions) as a result of the large beam size of the WMAP satellite. The WMAP free-free map is presented in Figure 1, indicating the location of each of the thirteen sources.

We use published radial velocity measurements together with GLIMPSE $8 \mu\text{m}$ images to better resolve and classify these star forming regions. This improves on our use of the catalogue of Russeil (2003) in Paper I. In other words, we classify star forming regions on the basis of kinematic distances (as determined through radial velocities towards known H II regions) and morphology seen in the 8 micron PAH bands.

We carried out a SIMBAD search for H II regions within each of the WMAP sources and compiled the associated hydrogen recombination line velocities.

Our morphological analysis was primarily conducted using the 3.1 by 2.4 degree Band 4 mosaic images from GLIMPSE (Benjamin et al. 2003). In many cases, these mosaics were insufficiently large to encompass the entire WMAP sources from Paper I. In these cases, adjacent images were mosaicked together using the Montage package. In cases where the sources were outside the GLIMPSE coverage, we substituted Band A mosaics from MSX (Price et al. 2001).

We use the 8 micron band because it is dominated

by PAH emission, which Cohen & Green (2001) have shown to trace the free-free emission reasonably well. We discuss and expand upon this relationship in depth in §5.2.

2.1. Definition of Star Forming Regions

We define star forming regions (SFRs) as subsets of WMAP sources having similar radial velocities ($\pm 15 \text{ km s}^{-1}$), copious $8 \mu\text{m}$ emission in Spitzer and/or MSX images, and finally, morphologies that are consistent with physical association, e.g., bubble, shell, or finger/pillar structures. In other words, star forming regions are bubbles identified by features correlated both in space and in velocity.

To determine the location and size of each of the star forming regions we overlaid the positions and velocities of the known H II regions onto the 8 micron mosaics of the region and visually inspected the result. An example classification based on morphology and velocity is shown in Figure 2.

Having determined the size and location of a star forming region, we calculated a median velocity from the measured velocities. A kinematic distance was then determined using the Clemens (1985) Galactic rotation curve. In cases where the kinematic distance is ambiguous, we used published absorption line data, where available, to determine if the region is at the “near” or “far” distance.

In the next section, we describe each of the “star-forming regions”. In the supplemental online material, we present tables of each of the known H II regions with positions and velocities that are associated with each of the star forming regions.

3. PROPERTIES OF STAR FORMING REGIONS

The combined analysis of the WMAP sources with the GLIMPSE image mosaics and the H II region velocities yields 40 star forming regions. Ten of the thirteen WMAP sources harbor multiple star forming regions; sources within the inner third of the Galaxy are found to be especially confused, with multiple SFRs. However, as already noted, combining morphology from the $8 \mu\text{m}$ PAH emission with the velocities of known H II regions allows for a reasonably clear view of the physical separations of the star forming regions.

These star forming regions have mean radii between an arcminute and a degree, and distances between 3 and 17 kiloparsecs. The angular sizes translate into physical radii between 3 to 75 parsecs. The Galactic distribution of the star forming regions is presented in Figure 3.

The majority of known H II regions in the star forming regions lie in shell-like structures traced by PAH emission in the Spitzer or MSX images. Most of the remainder are found in the centre of the SFR.

We interpret those H II regions lying on shell-like structures in one of two ways. In many cases it is clear that the H II region is simply swept up shell material illuminated by a central cluster. In other cases, however, the shell material is illuminated by young stars resulting from triggered star formation in the swept up shell, as described by Elmegreen (1998). In some cases, the triggered stars are blowing their own bubbles in the shell.

In many cases, we find a low level of emission towards the centre of the bubble or shell structure; we interpret

this as the evacuation of the material from the interior of the bubble.

Although a comprehensive search for known H II regions was conducted over each of the WMAP sources, not every emission feature in the 8 micron GLIMPSE image is associated with a radial velocity determination. In some cases, particularly bright PAH features in the GLIMPSE mosaics are not coincident with any radial velocity measurements, indicating that we are potentially missing star forming regions within the WMAP sources. We identify these regions in the description of each of the WMAP sources, and we suggest that further radial velocity measurements would be instructive. This does add an uncertainty in determining the true stellar population of such regions and we comment where this is the case. In some cases we believe that a significant star forming region has not been identified due to a lack of conclusive H II data.

We present our SFRs in Table 2 with the columns as follows: column (1) the catalogue number, columns (2) and (3) the position of the sources in Galactic coordinates, columns (4) and (5) the semimajor and semiminor axes of the regions in arcseconds, column (6) the position angle of the region, column (7) the median velocity in km s^{-1} , columns (8) and (9) the measured and corrected half-spread of velocities in km s^{-1} where sufficient H II regions are identified as associated with the star forming region, column (10) the distance to the region in kiloparsecs, column (11) the mean radius of the source in parsecs, column (12) the dynamical age of the region given the velocity spread, and column (13) the reference that resolves the distance ambiguity (where applicable). In cases where the kinematic distance ambiguity remains, we indicate the properties resulting from both distances in columns (10), (11), and (12). We refer to regions from this table as “SFR” followed by the catalogue number hereafter.

We present 8 micron images from GLIMPSE or MSX for each of the WMAP sources in Figures 4 to 16. On each of these images, the location and size of the WMAP source is indicated with a dotted ellipse, and the location of SFRs is indicated by a solid (red, in the online copy) ellipse. Each of these images is presented with a logarithmic stretch to highlight fainter morphological features.

While individual velocities towards H II regions may be known with great precision (generally to better than $\pm 1 \text{ km s}^{-1}$), velocities to the entire regions are determined with much less accuracy; the H II regions are randomly distributed (in angle) around sources. Further, some of the SFRs are associated with a very limited number of radial velocities measurements. In either case, the maximum error in the mean source velocity is constrained by our selection criteria that a region have a velocity spread no greater than $\pm 15 \text{ km s}^{-1}$. This maximal velocity error corresponds to an error in the kinematic distances of approximately 30%.

To estimate the half-velocity spread, Δv_m , we first require that a SFR have multiple velocity measurements available. Next, we require that there be a spread in the measured velocities greater than 3 km s^{-1} ; otherwise we suspect that what appear to be multiple velocity measurements are actually measurements of the same H II region (the Galactic coordinates are often not sufficiently

precise to discriminate between physically different versus apparently different sources). Given a region that satisfies these two criteria, we define the *measured* Δv_m as half the difference between the maximum and minimum radial velocity.

This parameter must be corrected for sampling effects; it is unlikely that the maximum and minimum velocity of an expanding region will be found in a random selection of H II regions. Further, since most of the known H II regions appear on the edges of (presumably expanding) shells, the component of the expansion velocity projected onto the radial velocity is expected to be smaller than unity. Thus the measured half-velocity spread would generally be an underestimate of the actual expansion velocities of the regions.

We correct the half-velocity spread by a geometric factor found by running a Monte Carlo simulation modeling the difference between the observed half-velocity spread and the actual expansion velocity with a given number of velocity observations. The mean correction factor is 2.0, 1.4 and 1.2 for 5, 10 and 15 velocity measurements respectively. The error on this factor ranges from a factor of 2 for 5 velocity measurements, to 15% for 15 measurements. The *corrected* half-velocity spreads, Δv_c , are also given in Table 2. For regions where less than 5 velocity measurements are available, no correction factor is applied as the Monte Carlo simulation shows that the result is unreliable. These regions do not have a corrected half-velocity spread presented. The measured half-velocity spreads for these regions should be treated as lower limits of the expansion velocity.

The dynamical age, τ_{dyn} , of the system is determined by dividing the mean radius of the regions by the half-velocity spread. The dynamical ages of all of the regions are below 10^7 years, consistent with the existence of massive main-sequence stars producing large amounts of ionizing luminosity.

The true age of each of these systems is an undetermined quantity but the selection criteria for these regions imposes some constraint on the ages. Specifically, these regions are selected as the most luminous in free-free emission, indicating the presence of massive O stars, specifically those with short main-sequence lifespans. In Paper I we showed that the total ionizing luminosity of a cluster with a standard initial stellar mass function rapidly decreases after the cluster reaches an age of 4 Myrs. This indicates that the majority of the ionizing luminosity in a young cluster is quenched even before the late-O stars evolve off the main sequence.

In SFRs where a discernible, closed bubble is illuminated with free-free or PAH emission, an upper limit to the true age exists. In SFRs with only a diffuse bubble structure there is an ambiguity; the bulk of the ionizing luminosity may come from a central cluster, or it may come from star clusters that have been triggered along the shell of the region evacuated by a central cluster. In the latter case, it would be incorrect to constrain the age of the region to be less than 4 Myrs. This circumstance is particularly relevant when searching for a central stellar cluster; if the age cannot be constrained to under 4 Myr, the most massive stars in the central cluster have already evolved off the main sequence, leaving more evolved objects rather than bright, blue main-sequence objects.

3.1. Bubbles

In many of these regions, we observe bubbles at a variety of scales. Some bubbles essentially enclose the associated star forming regions, while smaller bubbles often lie in the walls of larger bubbles. Many of the smaller bubbles are listed in Churchwell et al. (2006), but the larger bubbles, with radii larger than $10'$, have not been previously catalogued.

In Paper I, we find that each of the WMAP sources that we have selected require ionizing luminosities of $Q_0 > 10^{51} \text{ s}^{-1}$, consistent with young stellar populations with $M > 10^4 M_\odot$. Such massive clusters may drive superbubbles, a notion supported by the fact that the largest bubbles we find have mean radii approaching 50 pc.

We present a list of bubbles associated with each of the star forming regions in Table 3. The columns are as follows: column (1) the catalogue number, columns (2) and (3) the positions of the bubbles in Galactic coordinates, columns (4) and (5) the semimajor and semiminor axes of the bubbles in arcminutes, column (6) the position angle of the bubble, column (7) the associated star forming region from Table 2, column (8) the mean radius of the bubble in parsecs using the distances to the associated star forming regions, column (9) the morphology classification flag of the bubble, and column (10) the GLIMPSE bubble catalogue number from Churchwell et al. (2006). Where the kinematic distance ambiguity has not been resolved, the mean radius of both the near and far distances are indicated. The morphology classification flag is C if a nearly closed or complete shell is visible in the GLIMPSE 8 micron image, or B if the bubble appears to be broken or blown-out. The GLIMPSE bubble catalogue number is indicated where the bubble has a similar position, size and shape to the source indicated in Churchwell et al. (2006).

3.2. H II Region Radial Velocities

Finally, we list the individual H II region velocities for each of the identified star forming regions in Table 4, available as an online supplemental table. The columns are as follows: column (1) the associated star forming region from Table 2, column (2) the name of the H II region, columns (3) and (4) the positions of the region in Galactic coordinates, column (5) the velocity of the region with respect to LSR in km s^{-1} , and column (6) the reference from which the velocity was taken.

4. INDIVIDUAL WMAP SOURCES

4.1. G10 including the W31 region

This WMAP source is dominated by four seemingly disparate star forming regions (see Figure 4), although SFR 1 and 2 may be associated as they are both in W31 (Westerhout 1958). We begin with a discussion of these two regions.

SFR 1 and 2 contain the brightest PAH emission, although there is a significant 8 micron background over this entire WMAP source that we cannot clearly attribute to any of the 4 regions. In addition to being in W31, SFR 1 and 2 are also linked by their close angular proximity and similar radial velocities. We treat them as separate regions as they are each enclosed by their own shell structures. The high surface brightness

$8\mu\text{m}$ emission located in the centre of each of SFR 1 and 2 is indicative of a young central cluster that has not had time to evacuate its environment. This is consistent with the short dynamical time determined for SFR 1. Strong molecular line emission is found by Kim & Koo (2002), who conclude that there are active interactions between the forming stellar clusters and their parent molecular clouds. They also assume a closer distance, associated with the expanding 3 kpc arm of the Galaxy (with a distance of 6 kpc from LSR), but they do note that there is evidence that the region is at the further distance. Assuming the near distance, they estimate star cluster masses of $1.22 \times 10^4 M_\odot$ for SFR 1 and $3.11 \times 10^3 M_\odot$ for SFR 2.

The radio nebula G10.0-0.3 and associated soft gamma repeater are coincident with SFR 1 with a distance of 14.5 kpc, consistent with our distance (Corbel et al. 1997; Vasisht et al. 1995). Further, there exists a luminous blue variable with a total mass (single or binary) exceeding $190 M_\odot$ consistent with the further distance (van Kerkwijk et al. 1995; Eikenberry et al. 2004). The region also contains a soft-gamma repeater (Kulkarni & Frail 1993). Corbel & Eikenberry (2004) suggests that W31, specifically SFR 1, may be separable along the line of sight into a component in the 3 kpc spiral arm, and a component at 14.5 kpc. We find this to be consistent with SFR 1 being a massive young star forming cluster at a distance of 14.5 kpc, with shell-like structure evident in the north-west and south-east edges of the region. Adjusting the values of Kim & Koo (2002) for the further distance, clusters of masses $7.1 \times 10^4 M_\odot$ and $1.8 \times 10^4 M_\odot$ are required for SFR 1 and 2 respectively.

SFR 3 and 4 are distinctly separated from SFR 1 and 2 as they both have substantially different radial velocities; the difference in velocities being 60 km s^{-1} and 15 km s^{-1} respectively. We view SFR 3 as a smaller, closer star forming region than 1 and 2. SFR 4, however has the morphology of a blown out bubble. The distance to this region, 16.7 kpc, implies a large bubble size of 46 pc. The strong PAH illumination on the northwest side of the region is potentially a triggered star forming region from the expansion of the now blown out bubble. However, the bubble structure is illuminated along the shell in all but the south (in the proposed area of blowout), indicating that a central ionizing source still exists within the bubble that is illuminating the southeast side; the interior of the bubble appears evacuated. We infer that the central cluster is still sufficiently young to possess ionizing stars.

At the location $(l, b) = (10.7, -0.16)$, there appears to be a hole in the background level of PAH emission. There are no known H II regions within this hole, suggesting that this is an extinction effect. If this is an extinction effect at 8 microns, the column towards this region must be particularly large. We suspect that this is an infrared dark cloud (IRDC). In 2MASS (Skrutskie et al. 2006), there does not appear to be any significant void of background stars, indicating that this IRDC is sufficiently distant to have no effect on the local field star population, but is closer than the source of the PAH background in this region. More detailed study of this object is required to establish its existence, let alone determine its physical properties.

4.2. *G24 including the W41 and W42 Regions*

WMAP source G24 encompasses a particularly complicated region. It is one of the largest WMAP sources (spanning nearly 4 degrees in the Galactic plane) and contains both W41 and W42 (Westerhout 1958).

SFR 5 encompasses the supernova remnant W41. In the one square degree region surrounding W41, velocity measurements suggest the H II regions are caused by confusion of spatially separated H II regions (Leahy & Tian 2008), consistent with the 4 spiral arms along the line of sight in this direction. We find SFR 6 associated with one of the overlapping components. There is a second known supernova remnant, G22.7 -0.2 (van den Bergh 1978), also within SFR 5.

In addition to SFR 5 and 6, we identify 6 additional star forming regions within this WMAP source. For a number of these regions, specifically SFR 7, 9, and 12, the kinematic distance ambiguity remains. SFR 7 and 8 are easily distinguished by the presence of H II regions along their perimeters. There is a lack of strong central PAH illumination in both of these star forming regions, indicating that their centres have been evacuated. In addition, the rims of SFR 7 and 8 are not particularly bright in PAH emission, indicating that the hypothesized shell has dispersed or that the central cluster is no longer emitting ionizing radiation. Either circumstance implies that these two regions are older (> 4.5 Myr) and that the majority of the observed PAH and free-free emission is provided by triggered regions on the perimeter.

SFR 9 contains only a single H II region velocity in its centre, but exhibits a clear bubble morphology. SFR 10 is a much larger region, with a mean radius of 43 pc. While the brightest PAH regions lie towards the southwest side of the region, the north and eastern edges are defined by a clear shell structure. There is a H II region on the northern shell that has a similar velocity to those of the brighter regions to the southwest. In addition, there appears to be a central component to the PAH emission in this region at $(l, b) = (24.8^\circ, 0.1^\circ)$.

SFR 11 is associated with the W42 radio source but also includes an extended shell structure to the south and west of the original radio source with consistent velocity measurements along the shell. Lester et al. (1985) argue for the near galactic distance on the basis that there is minimal extinction towards the source in sulphur forbidden line emission, disregarding the known absorption velocities. Independent of the central source distance for the W42 region, an associated H II region at $(l, b) = (25.41^\circ, -0.25^\circ)$ is also determined to be at the near kinematic distance (Kolpak et al. 2003), hence we adopt this distance. Blum et al. (2000) find a central cluster with a single O5-6.5 star, indicating that this is comparable to a cluster a few times the mass of Trapezium, rather than something particularly massive.

SFR 12 is a more extended region outlined by a shell morphology its western edge. This bright PAH emission is associated with 2 similar H II region velocities. The overall size and shape of the region is suggested by the shell-like structure visible in the southeastern edge, but additional H II velocity measurements are required to ensure this structure is associated with the known H II regions.

4.3. *G30 including the W43 region*

While G30 is also a large region ($\sim 4^\circ$ along the major axis), it is reasonably simple. We identify 6 star forming regions within this WMAP source, SFR 13-18, but two are clearly dominant; SFR 17 associated with W43, and SFR 14.

SFR 17 consists of a bright central region with a shell outlined by a series of H II regions all at similar velocities. W43, located at $(l, b) = (30.75^\circ, -0.02^\circ)$, lies inside SFR 17. This central region has been identified as a ministarburst region with the detection of a cluster of Wolf-Rayet and OB stars, undergoing a second generation of star formation through the submillimeter observations of massive young stellar objects (Motte et al. 2003; Lester et al. 1985; Blum et al. 1999). We identify a much larger shell surrounding this region at similar radial velocities to the central complex. There is no obvious bubble associated with this SFR.

SFR 16, at $(l, b) = (30.54^\circ, 0.02^\circ)$, is contained completely inside and is much smaller than SFR 17. However, SFR 16 is distinguished by a significantly different radial velocity (44 vs. 99 km s $^{-1}$).

SFR 14 is located at a similar velocity to SFR 17, but is separated on the sky by an angle of $\sim 0.6^\circ$ and it is located at the far distance (8.7 kpc) while SFR 17 is located at near distance (6.3 kpc). SFR 14 resides in the same 8 micron background as SFR 17. It is known to be forming stars, as it contains a hot molecular core and is associated with a molecular cloud (Olmi et al. 2003; Pratap et al. 1999).

The remainder of the star forming regions within this WMAP source are low brightness sources in PAH emission and are not expected to contribute significantly to the total young stellar population.

4.4. *G34*

We identify 3 well separated star forming regions in G34, SFRs 19, 20 and 21. The dominant region is SFR 19, coincident with the majority of the background PAH emission in this area. At the heart of this star forming region is the cometary H II region G34.3+0.2 (Reid & Ho 1985). Outside the inner 10 arcminutes of the radio source, we find three bubble structures (identified as bubbles 22, 23 and 24), indicating that this region is composed of more than just the single O7V star assumed by Rodríguez-Rico et al. (2002).

SFR 21 is suggested primarily by its morphology, as only two H II region velocities are identified. The most prominent structure is on the east, where we identify a number of bubble-like objects. Our primary motivation in associating this large diffuse region together is the existence of structure all along the perimeter of the bubble, following the shell of the structure on the east. It is also possible that this region consists of two separate star forming regions, on the east and the west, but in that case it is unclear where the boundary between the two would be.

In Paper I, this WMAP source was assigned a distance of 10.5 kpc taken from Russeil (2003); this is consistent with our present estimate to the distance to SFR 21. However, from the PAH emission evident in the Spitzer image, the majority of the free-free emission may well be coming from SFR 19, located at a distance of only

2.2 kpc. This would reduce the ionizing luminosity of the region dramatically.

4.5. G37 including the W47 region

Two star forming regions have been identified in this WMAP region, both at similar velocities and exhibiting ring structure. SFR 22, which includes W47, is the larger source. There are 14 known H II regions, located in the upper half of the bubble. While the southern shell is more diffuse, we do not classify this bubble as blown out, as a wall is still visible in the PAH emission. Much diffuse PAH emission is visible outside this region but specifically towards the brighter regions on the northern shell, implying that the majority of the emission is due to the triggered regions on the shell wall rather than a central source. This suggests that the region is old. The uneven illumination of the shell structure further supports this assessment. W47, located on the northeastern shell of SFR 22, has not been extensively studied in the literature.

SFR 23 has similar radial velocities, but we are unaware of any resolution of the kinematic distance ambiguity in this case. A nearly circular shell structure is visible with a gap on the southeastern wall.

4.6. G49 including the W51 region

The region containing WMAP source G49 is a well studied area owing to the presence of W51. We identify two star forming regions within this source. The chaotic structure in the PAH emission indicates that these regions are particularly active and young. This chaotic structure makes it difficult to determine the actual shape and size of the star forming regions. In the case of SFR 25, the shape is motivated by shell structure on the northwestern edge. For SFR 24, the shape is motivated by the distribution of H II regions. In both cases, we suspect that the true extent of the star forming regions may be larger. The distances to these regions are similar, 5.6 kpc for SFR 24 and 5.7 kpc for SFR 25. These distances are consistent with the distance of 5.1 kpc determined through trigonometric parallax to W 51 IRS2 (Xu et al. 2009). Ultimately, we have separated these regions into two due to the separation of known H II regions into two clusters on the sky. The two regions have previously been separated in the literature, where SFR 24 is labelled W51B and SFR 25 is W51A.

W51 is a well known star formation region (Kang et al. 2009). Conti & Crowther (2004) separate SFR 25 into W51A and W51 West, placing them at a similar distance of 5.1 kpc. They determine an ionizing luminosity for both these sources of $Q_0 = 1.01 \times 10^{51}$ from ground based observations of the free-free flux. For SFR 24, they determine an ionizing luminosity of $Q_0 = 1.07 \times 10^{50}$. Adjusting for the difference in the presumed distance, the total ionizing luminosity from the three Conti & Crowther sources accounts for a quarter of the ionizing luminosity determined from the entire WMAP source. This is not surprising; as we indicated in Paper I, the bulk of the ionizing luminosity leaks beyond the more compact H II region defined by ground-based observations into the extended low density (ELD) region.

Figuerêdo et al. (2008) propose a smaller distance of 2.0 kpc to W51A based on the spectrophotometric distance

of a number of O stars observed in the region, in contrast to the extensive kinematic and now trigonometric parallax distances determined. In the spectral classification of their target stars, there were unable to determine the luminosity class and argue for ZAMS based on the presence of ongoing star formation indicating a young region. However we have determined the dynamical age of the system to be two million years, which is sufficient for the most massive of stars to evolve off the main sequence. Further, the difference in the smaller and larger distances corresponds to a difference of 2 in magnitude, which in turn corresponds reasonably to the difference between the K-band magnitudes of a mid-to-late O star from luminosity class V to I (Martins & Plez 2006). Thus a more consistent story is that the identified stars are actually supergiants at the original distance of the source, 5.1 kpc.

4.7. G283 including the NGC 3199, RCW 49 and Westerlund 2 regions

We identify one star forming region, SFR 26, in WMAP source G283. Unlike the regions closer to the Galactic centre, there is little confusion in this source. In fact, SFR 26 is similar in shape and size to the WMAP source. We use the MSX image in this region as only the eastern edge of this source has been included in the GLIMPSE survey.

SFR 26 is associated with NGC 3199 and RCW 49, both known regions of active star formation. NGC 3199, located towards the southwest of the WMAP source, is associated with the Wolf-Rayet star WR 18 (Deharveng & Maucherat 1974). We know of no in-depth attempt to find a cluster in this region.

RCW 49 is located in the northeast half of the WMAP region and is associated with the brightest patch of PAH emission within the WMAP source. RCW 49 is a well known massive star forming region with its embedded massive cluster Westerlund 2. For a review of this association, see §2 of Tsujimoto et al. (2007). Extensive surveys of the cluster have been completed in the infrared (Ascenso et al. 2007), and x-rays (Tsujimoto et al. 2007). Ascenso et al. (2007) find a total cluster mass of $7 \times 10^3 M_\odot$ using a distance of 2.8 kpc as compared to our distance of 4 kpc. This is a factor of four smaller than the estimate of the total stellar mass that we determine for the entire WMAP source using their distance. This indicates that a substantial number of stars associated with Westerlund 2 have evaded detection thus far and/or there is more than one substantial cluster associated with this star forming region.

4.8. G291 including the NGC 3603 and NGC 3576 regions

We find two overlapping star forming regions associated with the WMAP source found at G291; SFR 27 and 28. The separation of these two regions is motivated by the substantial difference in H II velocities. In SFR 27, the mean velocity is -22 km s^{-1} and extends to -16 km s^{-1} while SFR 28 has a mean velocity of 16 km s^{-1} and extends to 9 km s^{-1} . Note that the bright region associated with NGC 3576 at $(l, b) = (291.3^\circ, -0.7^\circ)$ in the shell of SFR 27 is projected to lie within SFR 28.

Persi et al. (1994) find a young massive cluster embedded in NGC 3576, detecting 40 cluster members with K band photometry. Barbosa et al. (2003) find a number of massive YSOs, indicating active star formation. NGC 3576 is located on the shell of the star forming region, suggesting that it may have been induced by a possible central cluster. This is consistent with the small size of the NGC 3576 region, indicating its youth.

SFR 28 is dominated by NGC 3603, located centrally within the region. Morphologically, it appears that material being swept up in the northwestern edge of the shell is triggering further star formation. This appears to also be the case at the location $(l, b) = (291.1^\circ, -0.75^\circ)$, which happens to overlap SFR 27. NGC 3603 is a known massive star forming region powered by HD 97950, often labelled a “starburst cluster” (for an extensive review see Melena et al. 2008). Conti & Crowther (2004) determine a total ionizing luminosity from NGC 3576 and NGC 3603 of $Q_0 = 3.4 \times 10^{51}$, similar to the ionizing luminosity for the entire WMAP source, $Q_0 = 4.2 \times 10^{51}$.

4.9. G298

G298 is an archetypal region of triggered star formation. We identify a single star forming region associated with this WMAP source, SFR 29. In this star forming region, we see an evacuated bubble with a continuous shell in the PAH emission, with elephant trunk structures and three possible locations of triggered star formation on the rim of the bubble; on the northeast, northwest, and southwest. A great deal of PAH emission is coming from north of the source, consistent with UV photons leaking out of the central bubble and illuminating further material, with the majority of material being closer to the galactic midplane.

Conti & Crowther (2004) identify only the northeast and northwest shell regions which they identify at $(l, b) = (298.227^\circ, -0.340^\circ)$ and $(l, b) = (298.862^\circ, -0.438^\circ)$, with a total ionizing luminosity of $Q_0 = 1.5 \times 10^{51}$, which is substantially smaller than the value we determine for the entire WMAP source, $Q_0 = 7.7 \times 10^{51}$. This larger ionizing luminosity implies that a truly massive cluster exists in this region, substantially larger than the two sources on the shell.

4.10. G311

The WMAP source G311 is a particularly large on the sky, stretching ~ 3 degrees along the Galactic plane, with a substantial PAH emission background. As this is a southern galactic plane source, it is not well studied, and we only identify three star forming regions convincingly, one of which appears to be dominating this area in the sky.

SFR 31 is central to both the WMAP source and the background PAH emission and has a large angular size (nearly 0.5°). Further it is outlined through its shell morphology as well as the presence of multiple known H II regions along the shell. For these reasons, we infer that it is the dominant star forming region within this WMAP source. SFR 30 is a much smaller bubble with a similar radial velocity measurement to SFR 31. However, the resolution of the kinematic distance ambiguity places SFR 30 at 3.5 kpc and SFR 31 at 7.4 kpc.

SFR 32 overlaps the southeastern edge of SFR 31, but is defined by H II regions having significantly different

radial velocities, placing it much further away (13.6 kpc versus 7.4 kpc).

The image shows a ridge in the PAH emission continuing from the southeast wall of SFR 31 strongly suggesting that it is associated with SFR 31. It is located from $(l, b) = (311.9^\circ, -0.2^\circ)$ to $(l, b) = (312.5^\circ, 0.1^\circ)$. However, there are no measured H II velocities for this feature, so we cannot confirm the association.

4.11. G327

All the H II region velocities in G327 lie within $\pm 13 \text{ km s}^{-1}$ of each other, so we identify only one star forming region, SFR 33. The morphology revealed by the PAH emission is rather complicated consisting of multiple bubbles. We interpret this region as an example of cascading star formation; an instance where multiple generations of triggered star formation occur in sequence. We find a large, diffuse shell, outlined by the red ellipse in Figure 14, with a number of known H II regions along the wall. Towards the south and the southwest of the shell, there are two additional clear bubble-like structures, identified as bubble 39 and 38 in Table 3. These both have additional H II regions visible on their walls. We interpret the largest region as a shell produced by an older central cluster. We speculate that the two smaller (younger?) bubbles were formed from clusters that were triggered by the original central cluster. These, in turn, are now triggering a third generation of star formation.

A previously identified source, G327.3-0.6 (Wyrowski et al. 2006), lies at the southern edge of SFR 33. This author identifies H II regions, hot cores and cold clumps. There is evidence that G327.3-0.6 was triggered by the expansion of the bubble on the south rim of SFR 33 (Minier et al. 2009).

We suggest that an older massive cluster should exist towards the centre of SFR 33 and may be visible in infrared surveys, as this region is not particularly distant (3.7 kpc).

4.12. G332

G332 is another large WMAP source (~ 3 degrees) with only two distinct clusters in H II radial velocities. SFR 34 is the dominant star forming region covering the majority of the WMAP source, while SFR 35 is a smaller region projected to lie in the interior of SFR 34.

The Spitzer image of SFR 34 is dominated by PAH-bright regions along the southeastern edge. The bright southeastern ridge includes RCW 106 right at the southeastern edge of the region to the region at $(l, b) = (333.6^\circ, -0.2^\circ)$.

4.13. G337

G337 is the widest WMAP source, spanning over 5 degrees in the Galactic plane. Five star forming regions are identified, SFR 35-40. All of the high surface brightness PAH emission in the Spitzer image lie within one of our star forming regions. There is a very prominent background diffuse PAH emission which is difficult to associate with a specific SFR. Each of the star forming regions are well separated both on the sky and by radial velocities. SFR 36, 38 and 40 lack strong central PAH emission suggesting that they have evacuated their surroundings. In contrast, SFR 37 and 39 show filled morphologies, suggestive of youth.

5. DISCUSSION

It has been noted before that regions with elevated free-free emission are associated with elevated PAH emission (Cohen & Green 2001; Murray & Rahman 2010). In Paper I, we used this correlation to argue that, based on the higher resolution 8 μm images, both the free-free and PAH emission are powered by a central source. In this paper, we have shown that bubbles are associated with all of the sources we have examined. The bubbles are identified by their bright rims as seen in PAH emission.

In addition, the bubbles are surrounded by an elevated background of PAH emission. The total luminosity in the 8 μm band of our WMAP sources is dominated by the elevated background as opposed to the high-surface brightness emission from the bubble walls. We conclude that the bulk of the ionizing photons from the central source escape through the bubble walls to reach distances of 100–200 pc or more, confirming the results of Paper I.

Previous estimates of stellar masses associated with giant H II regions have been underestimates of the total stellar mass at those locations. This follows from the fact that the H II regions reprocess only a small fraction of the ionizing photons in a given WMAP source.

We suggest that massive clusters inhabit the central regions of the bubbles. These clusters have evaded detection due to the lack of high surface brightness H II or radio continuum emission. We suggest that this results from a lack of gas and PAH particles in the immediate vicinity of the young clusters. The clusters have evacuated their surroundings, leaving little material to reprocess the ionizing photons emitted by the cluster.

5.1. Scale Height of O Stars

As discussed above, the WMAP sources studied in this paper are expected to contain approximately one-third of the O stars in the Galaxy. Using those objects in our catalogue with unique distances, we estimate the scale height of the O stars. As a first approximation, we assume that each of the star forming regions contain a similar number of O stars. Using this assumption, we construct the cumulative distribution function of star forming regions as a function of their height above the galactic plane. The scale height of the distribution is

$$h_* = 35 \pm 5 \text{ pc}. \quad (1)$$

This value is consistent with that obtained by Elias et al. (2006) for the local galactic disk (within 1 kpc) of $h_{\text{LGD}} = 34 \pm 3$ pc for their O-B2 subsample. Both are smaller than the value obtained by Reed (2000) of $h_{\text{LGD}} = 45 \pm 20$ pc for all OB stars within a distance of 4 kpc, but easily fall within their error bars. We note that the scale height of the molecular gas is $h \sim 40$ pc (Malhotra 1994).

5.2. Free-Free to PAH Emission Relationship

A morphological correlation between the MSX 8 micron emission and the radio continuum (Cohen & Green 2001). We investigate this correlation using the WMAP free-free emission maps and the PAH emission from the GLIMPSE 8 micron mosaics. For each WMAP source, we summed the free-free emission from the inside the Source Extractor ellipse from Paper I. We summed the

8 μm from the same ellipse in the Spitzer GLIMPSE mosaic. The result is shown in Figure 17. From a least-square fit, we find the following relationship:

$$F_{\text{PAH}} \propto F_{\text{ff}}^{2.0 \pm 0.34} \quad (2)$$

where F_{PAH} is the integrated 8 micron GLIMPSE flux and F_{ff} is the integrated 90 GHz free-free emission from the WMAP free-free foreground emission map. We find a similar relationship using the MSX Band A integrated flux in place of the GLIMPSE measurements.

5.3. Velocity Dispersion of the Molecular Gas

Both molecular and atomic gas in the disk of the Milky Way are seen to have supersonic velocity dispersions. These dispersions are normally interpreted as being due to turbulence, although their origin is uncertain. If the motions are due to turbulence, they must be driven, since undriven turbulence decays on roughly a dynamical time (Mac Low et al. 1998). Furthermore, the turbulence must be driven on 100 pc scales, since three dimensional turbulence cascades from large scales to small scales and not the other way around. A number of driving mechanisms have been proposed (Mac Low & Klessen 2004; Miesch & Bally 1994), including supernovae, stellar winds, and gravitational instabilities, with no conclusive evidence for any particular mechanism. We investigate the kinetic energy that is injected into the ISM by the expansion of the massive bubbles that we identify. We note that all of the star forming regions we have identified are likely to be in giant molecular clouds—a preliminary search shows that more than thirty are in fact in molecular clouds.

We calculate the mechanical luminosity in the expansion of each of the star forming regions using

$$L_{\text{mech}} = \frac{\pi}{2} \Sigma_0 \Delta v_c^3 r, \quad (3)$$

where $\Sigma_0 = 170 M_{\odot} \text{ pc}^{-2}$ (Solomon et al. 1987) is the surface density of a GMC, and r and Δv_c are taken from Table 2. For SFRs where the half-spread velocity was not measured, we used the mean half-spread velocity, $\Delta v = 12 \text{ km s}^{-1}$, of the known sources. For cases where the kinematic distance remains ambiguous, we take the mean radius of the region determined from both the near and far distances. Since the ratio of the two distances is less than two, this introduces an error of less than a factor of two for 9 out of our 40 SFRs. For each of the SFRs, we present the calculated dynamical properties in Table 5 with the columns as follows: column (1) the catalogue number, column (2) the mass swept up in the shell in solar masses, column (3) the kinetic energy of the swept up shell in erg, and column (4) the mechanical luminosity produced by the motion of the shell in erg s^{-1} .

The total mechanical luminosity being injected into the ISM inside the solar radius due to the expansion of these SFRs is the sum of the individual luminosities. We find

$$L_{\text{mech}} \approx 6.7 \times 10^{38} \left(\frac{\Sigma_0}{170 M_{\odot} \text{ pc}^{-2}} \right) \text{ erg s}^{-1}. \quad (4)$$

This sum encompasses only one-third of the star formation in the Galaxy. The other two-thirds should supply a proportionate amount of mechanical luminosity, for a total kinetic luminosity of $\sim 2 \times 10^{39} \text{ erg s}^{-1}$.

We compare this luminosity to that required to maintain the velocity dispersion in the molecular gas within the the solar circle:

$$L_{\text{turb}} \equiv \frac{1}{2} \frac{M v^3}{2h}, \quad (5)$$

where $h = 40$ pc is the scale height of the molecular disk, the molecular gas mass inside the solar circle $M = 1.0 \times 10^9 M_\odot$, and a molecular gas velocity $v = \sqrt{2 \ln 2} \sigma_{\text{mol}}$ with $\sigma_{\text{mol}} = 7 \text{ km s}^{-1}$ (Malhotra 1994). The turbulent luminosity is

$$L_{\text{turb}} \approx 2.4 \times 10^{39} \left(\frac{v}{8 \text{ km s}^{-1}} \right)^3 \text{ erg s}^{-1}. \quad (6)$$

We conclude that the mechanical luminosity we see in the bubbles, multiplied by a factor of three to account for the other two thirds of Galactic star formation, is sufficient to power the turbulent luminosity seen in the molecular gas.

We note that the kinetic energies calculated for most of the bubbles (refer to Table 5) range from 10^{48} to just below $10^{52} \text{ erg s}^{-1}$. The kinetic energies of our most energetic bubbles are similar to those measured in the superbubbles identified by Heiles (1979), which range from $4 \times 10^{51} \text{ erg s}^{-1}$ to $2 \times 10^{53} \text{ erg s}^{-1}$.

We note that our bubbles are selected by their ionizing luminosity, i.e., we require a very young stellar population. In addition, we do not see significant synchrotron radiation from these areas, indicating the absence of supernova remnants. This implies that the clusters are too young to have had more than a few supernova explode, and many of our sources likely have not had any supernovae go off. We infer that the superbubbles in the Galaxy are not initially driven by the energy from supernovae, but rather by the energy injected into the medium by the massive stars during their lifetime. It may well be, however, that supernovae contribute significantly to the kinetic energy later in the evolution of a superbubble.

5.4. Bubbles: Spherical Shells or Flattened Rings?

The three-dimensional geometry of the bubbles identified by Churchwell et al. (2006) has been contested recently. Beaumont & Williams (2010) propose that Churchwell et al.'s bubbles are flattened rings. Beaumont & Williams (2010) suggest that the aspect ratios of these rings may be anywhere from a few to as much as 10. Nineteen of our forty eight bubbles are in the GLIMPSE bubble catalogs. We test the assertion of Beaumont & Williams (2010) statistically using the bubbles in Table 3.

We model our bubbles as ellipsoids, following the procedure of Nourmeir (1999) with semi-axes a, b, c aligned along the x, y and z axes such that $a \geq b \geq c$. The matrix equation for the ellipsoid is

$$u^T X u = 1 \quad (7)$$

where u is an arbitrary position vector. The matrix X is a diagonal matrix with entries a^2, b^2, c^2 , corresponding to the semi-axes of the ellipsoid. We rotate the ellipsoid along the z-axis by an angle θ , and along the y-axis by an angle ϕ , producing the matrix

$$X' = \begin{bmatrix} \alpha \cos^2 \phi + c^2 \sin^2 \phi & \beta \cos \phi \cos \theta \sin \theta & (c^2 - \alpha) \sin \phi \cos \phi \\ \beta \cos \phi \cos \theta \sin \theta & a^2 \sin^2 \theta + b^2 \cos^2 \theta & -\beta \sin \phi \cos \theta \sin \theta \\ -(\alpha + c^2) \sin \phi \cos \phi & -\beta \sin \phi \cos \theta \sin \theta & \alpha \sin^2 \phi + c^2 \cos^2 \phi \end{bmatrix} \quad (8)$$

where we define $\alpha = a^2 \cos^2 \theta + b^2 \sin^2 \theta$, and $\beta = a^2 - b^2$.

To determine the observed ellipse on the sky resulting from the rotation of the ellipsoid, we produce an orthographic projection of the ellipsoid onto the y-z plane. The resulting projection is

$$X_P = \begin{bmatrix} a^2 \sin^2 \theta + b^2 \cos^2 \theta & -\beta \sin \phi \cos \theta \sin \theta \\ -\beta \sin \phi \cos \theta \sin \theta & \alpha \sin^2 \phi + c^2 \cos^2 \phi \end{bmatrix} \quad (9)$$

To minimize the observed axis ratio, we assume the bubbles are circular rings with $a = b$, implying the semi-major axis of the projected bubble is a , and the projected semi-minor axis is $\sqrt{a^2 \sin^2 \phi + c^2 \cos^2 \phi}$. The resulting axis ratio, a function of only the rotation along the y-axis, is given as

$$R_{ax}(\phi) = \frac{a}{\sqrt{a^2 \sin^2 \phi + c^2 \cos^2 \phi}} \quad (10)$$

We compute the expectation value of the axis ratio $\langle R_{ax}(a/c) \rangle$, for $a/c = 10$ and $a/c = 4$. Using eqn. (10) we find $\langle R_{ax}(10) \rangle = 2.4$ and $\langle R_{ax}(4) \rangle = 1.8$. We compare this to our sample of 48 bubbles, for which we find $\langle R_{ax} \rangle = 1.3 \pm 0.3$, suggesting that the intrinsic aspect ratio $a/c \lesssim 4$ at the two sigma level. In fact $\langle R_{ax} \rangle = 1.3$ corresponds to a mean intrinsic aspect ratio $a/c = 1.7$.

A more sensitive test is that of the maximum aspect ratio; the maximum observed aspect ratio is 2.2, corresponding to a maximum inclination angle of 31° from the face-on position of a ring with $a/c = 4$. For a simple random distribution of inclination angles, we would expect 48%, or 23 ± 7 of the bubbles to have an aspect ratio greater than 2.2.

We note that if the observed maximum aspect ratio (2.2) is in fact the true mean aspect ratio, then $\langle R_{ax}(2.2) \rangle = 1.4$, consistent with the observed mean aspect ratio.

We find an insufficient number of observed bubbles with large aspect ratios to support the geometry of a flattened ring and the original picture of nearly-spherical shells is more likely to be physically correct.

6. SUMMARY

From an analysis of the 13 most luminous sources found in the WMAP free-free emission map, we have identified 40 star forming regions using a combination of morphology in PAH emission from the Spitzer GLIMPSE and MSX surveys and velocities of known H II regions at the same location on the sky. For all 31 of the 40 regions we are able to determine a unique distance associated with the radial velocity measurements, allowing us to determine the physical size of these regions. For 20 of these star forming regions, there are a sufficient number of H II region velocity measurements to estimate the expansion speed of the region and consequently, a dynamical age.

We catalogue 48 bubble-like objects, 19 of which have been previously catalogued by Churchwell et al. (2006). For most of these bubbles, we were able to determine

a physical size. We also present a comprehensive list of the radio recombination line velocity measurements associated with each star forming region.

We discuss each of the WMAP sources individually, commenting on the morphology within the source. Many of the northern sky star forming regions are associated with previously identified star forming regions. In most cases, the previous masses (or luminosities) for embedded clusters are substantially underestimated, as earlier studies often did not take into account the leakage of ionizing photons from the central ionizing source. We also find substantial evidence of triggered star formation in many of the star forming regions. A number of our star forming regions, especially the southern sky regions, have not been previously investigated or identified as possible locations of massive stellar clusters.

We determine the scale height of the Galactic O stars to be $h_* = 35 \pm 5$ pc, consistent with previous values for the scale height of OB stars in the local galactic plane. We determine a strong empirical relationship between the total integrated PAH and free-free emission; $F_{\text{PAH}} \propto F_{\text{ff}}^2$.

We show that the kinetic energy injected per unit time into the galactic medium by the expansion of the star forming regions is similar to that required to maintain the velocity dispersion seen in the Galactic molecular gas. Thus we propose that the expansion of the star forming regions is a primary driver of turbulence in the molecular gas of the Galaxy. We further show that the kinetic energy of the identified bubbles is similar to that of known superbubbles, implying that superbubbles are being produced before any supernova activity has taken place within the cluster.

Finally, we show that the three dimensional geometry of the bubbles is more consistent with a nearly-spherical shell rather than a flattened ring geometry based on statistics of the identified sample.

We have benefited from greatly from ongoing discussions with C. Matzner, D-S. Moon, P. G. Martin, and R. Breton. This work is based [in part] on observations made with the Spitzer Space Telescope, which is operated by the Jet Propulsion Laboratory, California Institute of Technology under a contract with NASA. This research has made use of the SIMBAD database, operated at CDS, Strasbourg, France. This research made use of data products from the Midcourse Space Experiment. Processing of the data was funded by the Ballistic Missile Defense Organization with additional support from NASA Office of Space Science. This research has also made use of the NASA/IPAC Infrared Science Archive, which is operated by the Jet Propulsion Laboratory, California Institute of Technology, under contract with the National Aeronautics and Space Administration. This research made use of Montage, funded by the National Aeronautics and Space Administration's Earth Science Technology Office, Computation Technologies Project, under Cooperative Agreement Number NCC5-626 between NASA and the California Institute of Technology. Montage is maintained by the NASA/IPAC Infrared Science Archive. N.M. is supported in part by the Canada Research Chair program and by NSERC of Canada.

REFERENCES

- Anantharamaiah, K. R. 1985a, *Journal of Astrophysics and Astronomy*, 6, 177
 —. 1985b, *Journal of Astrophysics and Astronomy*, 6, 203
 Ascenso, J., Alves, J., Beletsky, Y., & Lago, M. T. V. T. 2007, *A&A*, 466, 137
 Barbosa, C. L., Damineli, A., Blum, R. D., & Conti, P. S. 2003, *AJ*, 126, 2411
 Beaumont, C. N., & Williams, J. P. 2010, *ApJ*, 709, 791
 Benjamin, R. A., et al. 2003, *PASP*, 115, 953
 Bennett, C. L., et al. 2003a, *ApJS*, 148, 97
 —. 2003b, *ApJS*, 148, 97
 Blum, R. D., Conti, P. S., & Damineli, A. 2000, *AJ*, 119, 1860
 Blum, R. D., Damineli, A., & Conti, P. S. 1999, *AJ*, 117, 1392
 Bronfman, L., Nyman, L., & May, J. 1996, *A&AS*, 115, 81
 Caswell, J. L. 1972, *Australian Journal of Physics*, 25, 443
 Caswell, J. L., & Haynes, R. F. 1987, *A&A*, 171, 261
 Caswell, J. L., Murray, J. D., Roger, R. S., Cole, D. J., & Cooke, D. J. 1975, *A&A*, 45, 239
 Churchwell, E., Walmsley, C. M., & Cesaroni, R. 1990, *A&AS*, 83, 119
 Churchwell, E., et al. 2006, *ApJ*, 649, 759
 Clark, J. S., Negueruela, I., Crowther, P. A., & Goodwin, S. P. 2005, *A&A*, 434, 949
 Clark, J. S., et al. 2009, *A&A*, 498, 109
 Clemens, D. P. 1985, *ApJ*, 295, 422
 Cohen, M., & Green, A. J. 2001, *MNRAS*, 325, 531
 Conti, P. S., & Crowther, P. A. 2004, *MNRAS*, 355, 899
 Corbel, S., & Eikenberry, S. S. 2004, *A&A*, 419, 191
 Corbel, S., Wallyn, P., Dame, T. M., Durouchoux, P., Mahoney, W. A., Vilhu, O., & Grindlay, J. E. 1997, *ApJ*, 478, 624
 Davies, B., Figer, D. F., Kudritzki, R., MacKenty, J., Najarro, F., & Herrero, A. 2007, *ApJ*, 671, 781
 Deharveng, L., & Maucherat, M. 1974, *A&A*, 34, 465
 Downes, D., Wilson, T. L., Bieging, J., & Wink, J. 1980, *A&AS*, 40, 379
 Eikenberry, S. S., et al. 2004, *ApJ*, 616, 506
 Elias, F., Cabrera-Caño, J., & Alfaro, E. J. 2006, *AJ*, 131, 2700
 Elmegreen, B. G. 1998, in *Astronomical Society of the Pacific Conference Series*, Vol. 148, *Origins*, ed. C. E. Woodward, J. M. Shull, & H. A. Thronson Jr., 150+
 Figer, D. F., Kim, S. S., Morris, M., Serabyn, E., Rich, R. M., & McLean, I. S. 1999, *ApJ*, 525, 750
 Figer, D. F., MacKenty, J. W., Robberto, M., Smith, K., Najarro, F., Kudritzki, R. P., & Herrero, A. 2006, *ApJ*, 643, 1166
 Figuerêdo, E., Blum, R. D., Damineli, A., Conti, P. S., & Barbosa, C. L. 2008, *AJ*, 136, 221
 Gardner, F. F., & Whiteoak, J. B. 1978, *MNRAS*, 183, 711
 Georgelin, Y. P., & Georgelin, Y. M. 1970, *A&A*, 7, 133
 Gold, B., et al. 2009, *ApJS*, 180, 265
 Harper-Clark, E., & Murray, N. 2009, *ApJ*, 693, 1696
 Heiles, C. 1979, *ApJ*, 229, 533
 Ho, L. C. 1997, in *Revista Mexicana de Astronomia y Astrofisica Conference Series*, Vol. 6, *Revista Mexicana de Astronomia y Astrofisica Conference Series*, ed. J. Franco, R. Terlevich, & A. Serrano, 5+
 Ikeda, M., Ohishi, M., Nummelin, A., Dickens, J. E., Bergman, P., Hjalmarsen, Å., & Irvine, W. M. 2001, *ApJ*, 560, 792
 Kang, M., Bieging, J. H., Povich, M. S., & Lee, Y. 2009, *ApJ*, 706, 83
 Kim, K., & Koo, B. 2001, *ApJ*, 549, 979
 —. 2002, *ApJ*, 575, 327
 Kolpak, M. A., Jackson, J. M., Bania, T. M., Clemens, D. P., & Dickey, J. M. 2003, *ApJ*, 582, 756
 Kuchar, T. A., & Bania, T. M. 1994, *ApJ*, 436, 117
 Kulkarni, S. R., & Frail, D. A. 1993, *Nature*, 365, 33
 Leahy, D. A., & Tian, W. W. 2008, *AJ*, 135, 167
 Lester, D. F., Dinerstein, H. L., Werner, M. W., Harvey, P. M., Evans, II, N. J., & Brown, R. L. 1985, *ApJ*, 296, 565
 Lockman, F. J. 1976, *ApJ*, 209, 429
 —. 1989, *ApJS*, 71, 469
 Lockman, F. J., Pisano, D. J., & Howard, G. J. 1996, *ApJ*, 472, 173
 Mac Low, M., & Klessen, R. S. 2004, *Reviews of Modern Physics*, 76, 125

- Mac Low, M., Klessen, R. S., Burkert, A., & Smith, M. D. 1998, *Physical Review Letters*, 80, 2754
- Malhotra, S. 1994, *ApJ*, 433, 687
- Martins, F., & Plez, B. 2006, *A&A*, 457, 637
- Melena, N. W., Massey, P., Morrell, N. I., & Zangari, A. M. 2008, *AJ*, 135, 878
- Miesch, M. S., & Bally, J. 1994, *ApJ*, 429, 645
- Minier, V., et al. 2009, *A&A*, 501, L1
- Motte, F., Schilke, P., & Lis, D. C. 2003, *ApJ*, 582, 277
- Murray, N., & Rahman, M. 2010, *ApJ*, 709, 424
- Nakanishi, H., & Sofue, Y. 2006, *PASJ*, 58, 847
- Noumeir, R. 1999, *Pattern Recognition Letters*, 20, 585
- Olmi, L., Cesaroni, R., Hofner, P., Kurtz, S., Churchwell, E., & Walmsley, C. M. 2003, *A&A*, 407, 225
- Palagi, F., Cesaroni, R., Comoretto, G., Felli, M., & Natale, V. 1993, *A&AS*, 101, 153
- Persi, P., Roth, M., Tapia, M., Ferrari-Toniolo, M., & Marenzi, A. R. 1994, *A&A*, 282, 474
- Pestalozzi, M. R., Minier, V., & Booth, R. S. 2005, *A&A*, 432, 737
- Pratap, P., Megeath, S. T., & Bergin, E. A. 1999, *ApJ*, 517, 799
- Price, S. D., Egan, M. P., Carey, S. J., Mizuno, D. R., & Kuchar, T. A. 2001, *AJ*, 121, 2819
- Quiroza, C., Rood, R. T., Balser, D. S., & Bania, T. M. 2006, *ApJS*, 165, 338
- Reed, B. C. 2000, *AJ*, 120, 314
- Reid, M. J., & Ho, P. T. P. 1985, *ApJ*, 288, L17
- Rodríguez-Rico, C. A., Rodríguez, L. F., & Gómez, Y. 2002, *Revista Mexicana de Astronomía y Astrofísica*, 38, 3
- Russeil, D. 2003, *A&A*, 397, 133
- Russeil, D., Adami, C., Amram, P., Le Coarer, E., Georgelin, Y. M., Marcelin, M., & Parker, Q. 2005, *A&A*, 429, 497
- Sewilo, M., Watson, C., Araya, E., Churchwell, E., Hofner, P., & Kurtz, S. 2004, *ApJS*, 154, 553
- Skrutskie, M. F., et al. 2006, *AJ*, 131, 1163
- Solomon, P. M., Rivolo, A. R., Barrett, J., & Yahil, A. 1987, *ApJ*, 319, 730
- Tsujimoto, M., et al. 2007, *ApJ*, 665, 719
- van den Bergh, S. 1978, *ApJS*, 38, 119
- van Kerkwijk, M. H., Kulkarni, S. R., Matthews, K., & Neugebauer, G. 1995, *ApJ*, 444, L33
- Vasisht, G., Frail, D. A., & Kulkarni, S. R. 1995, *ApJ*, 440, L65
- Walsh, A. J., Hyland, A. R., Robinson, G., & Burton, M. G. 1997, *MNRAS*, 291, 261
- Westerhout, G. 1958, *Bull. Astron. Inst. Netherlands*, 14, 215
- Wilson, T. L., Mezger, P. G., Gardner, F. F., & Milne, D. K. 1970, *A&A*, 6, 364
- Wink, J. E., Altenhoff, W. J., & Mezger, P. G. 1982, *A&A*, 108, 227
- Wink, J. E., Wilson, T. L., & Bieging, J. H. 1983, *A&A*, 127, 211
- Wood, D. O. S., & Churchwell, E. 1989, *ApJS*, 69, 831
- Wyrowski, F., Menten, K. M., Schilke, P., Thorwirth, S., Güsten, R., & Bergman, P. 2006, *A&A*, 454, L91
- Xu, Y., Reid, M. J., Menten, K. M., Brunthaler, A., Zheng, X. W., & Moscadelli, L. 2009, *ApJ*, 693, 413

Table 1
WMAP Source List

Name	l (deg)	b (deg)	s_{maj} (deg)	s_{min} (deg)	PA (deg)	S_{ff} (Jy)	Luminosity Rank	Notes
G10	10.4	-0.3	0.61	0.44	-21.2	86	12	W31
G24	24.5	0	1.96	0.83	-7.2	1377	10, 11	W41, W42
G30	30.5	0	2.27	0.95	2.7	1585	3, 8	W43
G34	34.7	-0.2	0.92	0.57	6.1	285	6	...
G37	37.6	0	0.8	0.71	-59.9	244	13	W47
G49	49.3	-0.3	0.99	0.55	-13.5	458	9	W51
G283	283.9	-0.6	1.37	0.78	-32.1	848	15	NGC 3199, RCW49, Partial GLIMPSE Coverage
G291	291.2	-0.7	1.04	0.75	-31.1	688	14	NGC 3603, NGC3576, No GLIMPSE Coverage
G298	298.4	-0.4	0.91	0.73	-37.3	313	5	...
G311	311.6	0.1	1.72	0.93	6.5	766	16	...
G327	327.5	-0.2	1.55	0.83	-10.7	943	17	...
G332	332.9	-0.3	1.56	0.93	-3.3	1787	7	...
G337	337.3	-0.1	2.58	1.2	-8.9	2239	2, 4	...
...	359.9	-0.1	1.2	0.51	-3	1105	1	Galactic Centre region, exluded from analysis

Note. — The luminosity rank indicates the ranking of the source with respect to the ionizing luminosity produced, with multiple ranks indicating sources that were divided in Paper I. The free-free flux is measured in the W band at 90 GHz from the WMAP Free-Free Foreground Emission Map (Bennett et al. 2003b).

Table 2
Star Forming Region Parameters

#	l (deg)	b (deg)	sma _j (arcmin)	smin (arcmin)	PA (deg)	v_{LSR} (km s ⁻¹)	Δv_m (km s ⁻¹)	Δv_c (km s ⁻¹)	D (kpc)	$\langle R \rangle$ (pc)	t_{dyn} (Myr)	KDA Ref.
1	10.156	-0.384	7.4	4.3	27	15	15	24	14.5	25	1.0	3
2	10.288	-0.136	6.8	4.4	89	10	15.2	25	...	3
3	10.450	0.021	3.3	2.4	54	69	6.1	5	...	1
4	10.763	-0.498	11.7	7.3	55	-1	16.7	46	...	1
5	22.991	-0.345	17.3	14.2	-16	76	4.9, 10.8	22, 49
6	23.443	-0.237	2.1	1.8	90	104	9.2	5	...	1
7	23.846	0.152	8.9	4.9	8	95	17	27	5.8, 9.8	12, 20	0.4, 0.7	...
8	24.050	-0.321	26.1	14.5	-9	85	17	24	10.3	61	2.6	3
9	24.133	0.438	2.9	2.3	0	98	5.9, 9.7	4, 7
10	24.911	0.134	26.7	21.8	0	100	15	21	6.1	43	2.1	3
11	25.329	-0.275	7.5	5.0	90	63	4	8	4.1	7	0.9	7
12	25.992	0.119	18.4	11.4	0	106	4	...	6.5, 8.8	28, 38	7.0, 9.5	...
13	28.827	-0.230	1.4	1.1	22	88	5	...	5.3	2	0.4	4
14	29.926	-0.049	5.4	5.2	0	97	8.7	13	...	1
15	30.456	0.443	3.0	2.6	0	58	3.6, 11	3, 9
16	30.540	0.022	1.0	0.8	-48	44	5	...	11.9	3	0.6	4
17	30.590	-0.024	23.9	14.3	0	99	7	8	6.3	35	4.2	2
18	32.162	0.038	5.3	4.7	0	96	8.2	12	...	2
19	34.243	0.146	9.2	7.1	-13	37	2.2	5	...	2
20	35.038	-0.490	3.8	2.4	76	51	3	3	...	1
21	35.289	-0.073	26.6	12.5	0	48	11	62	...	2
22	37.481	-0.384	24.8	23.8	0	50	13	17	10.5	74	4.4	2
23	38.292	-0.021	9.8	9.4	0	57	3.5, 9.9	10, 28
24	49.083	-0.306	8.9	4.7	0	68	4	6	5.6	11	2.0	...
25	49.483	-0.343	13.9	8.0	69	60	10	13	5.7	18	1.4	...
26	283.883	-0.609	66.6	41.3	-28	0	15	20	4	63	3.2	5
27	290.873	-0.742	36.6	25.8	90	-22	6	10	3	27	2.8	...
28	291.563	-0.569	34.4	27.4	-25	16	7	11	7.4	67	6.3	...
29	298.505	-0.522	24.7	24.2	0	24	7	11	9.7	69	6.2	...
30	310.985	0.409	3.2	2.8	90	-51	3.5	3	...	6
31	311.513	-0.027	27.5	25.0	90	-55	10	13	7.4	56	4.3	6
32	311.650	-0.528	9.0	5.4	90	34	13.6	29
33	327.436	-0.058	34.9	31.7	0	-60	13	17	3.7	36	2.1	6
34	332.809	-0.132	48.6	30.2	0	-52	6	7	3.4	39	5.9	6
35	333.158	-0.076	2.5	1.9	90	-91	5.5, 9.7	4, 6
36	336.484	-0.219	4.1	3.3	-60	-88	6	10	5.4, 10.2	6, 11	0.6, 1.2	...
37	336.971	-0.019	19.0	11.8	31	-74	7	10	10.9	49	5.0	6
38	337.848	-0.205	22.1	13.8	-16	-48	7	9	3.5	18	2.0	6
39	338.412	0.120	6.6	3.1	68	-33	4	4	2.5, 13.3	4, 19	1.0, 4.8	...
40	338.888	0.618	10.1	6.9	25	-63	4.4	11	...	6

References. — (1) Churchwell et al. (1990); (2) Kuchar & Bania (1994); (3) Sewilo et al. (2004); (4) Palagi et al. (1993); (5) Wilson et al. (1970); (6) Caswell & Haynes (1987); (7) Kolpak et al. (2003)

Note. — The KDA Ref indicates the source by which the kinematic distance ambiguity is resolved. In cases where no reference is given, the kinematic distance is either unique or we present the near and far distances.

Table 3
Bubble-like Objects Associated with the Star Forming Regions

#	l (deg)	b (deg)	sma _j (arcmin)	smin (arcmin)	PA (deg)	Associated SF Region	$\langle R \rangle$ (pc)	Classification Flag	GLIMPSE Bubble
1	10.316	-0.137	1.6	1.2	50	2	6.1	C	...
2	10.763	-0.498	11.7	7.3	55	4	46	B	N2
3	23.703	0.166	0.3	0.3	66	7	0.5, 0.9	C	...
4	23.873	-0.114	0.6	0.4	-76	8	1.5	C	...
5	23.880	-0.350	0.4	0.3	69	8	1.0	C	...
6	23.904	0.070	0.4	0.4	90	7	0.7, 1.2	C	N32
7	24.050	-0.321	26.1	14.5	-9	8	61	C	...
8	24.095	0.456	0.8	0.7	-52	9	1.3, 2.1	C	...
9	24.133	0.438	2.9	2.3	0	9	4.5, 7.3	B	...
10	24.505	0.240	5.4	3.1	-50	10	7.5	B	N35
11	24.840	0.106	4.6	2.1	-64	10	5.9	B	N36
12	25.292	0.296	2.2	1.5	90	10	3.3	B	N37
13	25.323	-0.293	5.4	5.4	0	11	6.4	B	...
14	25.992	0.119	18.4	11.4	0	12	28, 38	B	...
15	26.112	-0.030	2.4	2.0	0	12	4.2, 5.6	B	...
16	28.827	-0.230	1.4	1.1	22	13	1.9	C	N49
17	30.456	0.443	3.0	2.6	0	15	2.9, 9.0	C	...
18	30.612	-0.194	11.0	5.8	0	17	15	B	...
19	30.736	-0.022	3.0	2.1	-36	17	4.7	C	N52
20	32.098	0.090	1.0	0.8	-43	18	2.1	C	N55
21	32.159	0.039	4.6	4.0	0	18	10	C	...
22	34.156	0.145	3.8	2.6	11	19	2.0	B	N61
23	34.296	0.077	2.0	1.9	90	19	1.2	B	...
24	34.331	0.213	1.7	1.5	-38	19	1.0	B	N62
25	35.002	-0.130	5.1	3.2	-68	21	13	B	...
26	35.032	-0.482	1.6	1.4	54	20	1.3	B	...
27	35.259	0.119	0.5	0.4	-28	21	1.5	C	N66
28	35.642	-0.059	5.8	2.9	-75	21	14	C	N68
29	37.481	-0.384	24.8	23.8	0	22	74	B	...
30	38.293	-0.015	8.1	7.4	0	23	7.9, 22	B	N71
31	38.352	-0.133	1.0	0.9	0	23	1.0, 2.8	B	N72
32	298.218	-0.323	2.4	1.7	90	29	5.8	C	S181
33	298.527	-0.562	18.5	14.7	-51	29	47	C	...
34	310.985	0.409	3.2	2.8	90	30	3.1	C	S137
35	311.487	0.401	2.5	1.7	12	31	4.6	B	S133
36	311.495	-0.013	24.2	17.7	-72	31	45	B	...
37	311.916	0.222	2.2	1.4	-73	31	3.9	C	...
38	326.882	-0.389	13.1	8.0	-66	33	11	B	...
39	327.532	-0.605	14.9	14.1	0	33	16	B	...
40	333.158	-0.076	2.5	1.9	90	35	3.6, 6.3	B	...
41	336.484	-0.219	4.1	3.3	-60	36	5.8, 11	C	...
42	336.778	0.089	2.9	2.4	-20	37	8.4	B	...
43	336.853	-0.016	1.6	1.2	82	37	4.5	B	...
44	336.887	0.059	2.7	1.6	0	37	6.8	B	...
45	336.921	-0.195	2.2	1.9	-70	37	6.4	C	...
46	337.153	-0.178	1.8	1.6	68	37	5.4	B	...
47	337.676	-0.335	2.1	1.8	35	38	2.0	C	S37
48	338.891	0.596	3.7	3.0	-55	40	4.3	B	S29

Note. — The classification flag refers to the morphology of the bubble: 'C' indicates that the bubble is a closed bubble and 'B' refers to a broken bubble. The GLIMPSE bubble column indicates the identification of this bubble in Churchwell et al. (2006) with the catalogue number.

Table 4
H II Region Velocities

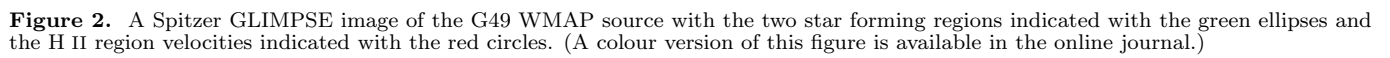
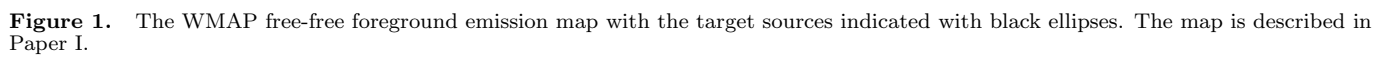
Associated Star Forming Region	Name	l (deg)	b (deg)	v_{LSR} (km s ⁻¹)	Reference Number
1	[L89b] 10.073-00.412	10.0732	-0.4119	13.6	1
...	GRS 010.20 -00.30	10.1467	-0.3377	13	2
...	[WMG70] 010.2-00.3	10.149	-0.343	14.2	3
...	PMN J1809-2019	10.1589	-0.3489	14.2	1
...	GAL 010.2-00.3	10.1615	-0.3546	12.8	4
...	[L89b] 10.190-00.426	10.1898	-0.426	36.2	1
...	[L89b] 10.190-00.426	10.1898	-0.426	5.4	1
2	[WC89] 010.30-0.15B	10.303	-0.1462	7.7	5
...	GAL 010.32-00.16	10.3148	-0.15	13.1	4
3	GAL 010.46+00.02	10.458	0.0239	70.1	1
...	GAL 010.46+00.03	10.4625	0.034	68.9	4
...	GAL 010.47+00.03	10.4722	0.0264	68	6
4	GAL 010.6-00.4	10.6205	-0.3872	0.2	7
...	[SG70] 010.6-0.4	10.6258	-0.383	0.4	8
...	[KC97c] G010.7-00.5	10.6639	-0.4666	-2.4	1

References. — (1) Lockman (1989); (2) Anantharamaiah (1985a); (3) Wilson et al. (1970); (4) Bronfman et al. (1996); (5) Kim & Koo (2001); (6) Wood & Churchwell (1989); (7) Wink et al. (1982); (8) Lockman et al. (1996); (9) Quireza et al. (2006); (10) Kolpak et al. (2003); (11) Caswell (1972); (12) Wink et al. (1983); (13) Pestalozzi et al. (2005); (14) Kuchar & Bania (1994); (15) Walsh et al. (1997); (16) Rodríguez-Rico et al. (2002); (17) Caswell & Haynes (1987); (18) Georgelin & Georgelin (1970); (19) Russeil et al. (2005); (10) Ikeda et al. (2001); (21) Gardner & Whiteoak (1978); (22) Caswell et al. (1975); (23) Downes et al. (1980)

Note. — Table 4 is published in its entirety in the electronic edition of the Astrophysical Journal. A portion is shown here for guidance regarding its form and content.

Table 5
Dynamical Properties of the Star
Forming Regions

SFR #	$\log M_{sh}$ (M_{\odot})	$\log E_k$ (erg)	$\log L_{mech}$ (erg s^{-1})
1	4.9	50.7	37.8
2	4.9	50.1	36.9
3	2.8	48.0	36.2
4	5.7	50.9	37.2
5	5.4	50.5	37.1
6	2.9	48.1	36.2
7	4.3	50.2	37.7
8	6.1	51.8	38.1
9	2.9	48.1	36.2
10	5.6	51.3	37.8
11	3.3	48.1	35.8
12	5.3	49.5	35.6
13	1.6	46.0	34.6
14	4.1	49.3	36.6
15	3.1	48.2	36.3
16	2.2	46.6	34.8
17	5.4	50.2	36.6
18	4.0	49.1	36.6
19	2.9	48.0	36.2
20	2.0	47.2	35.9
21	6.1	51.3	37.3
22	6.3	51.8	37.8
23	4.6	49.7	36.8
24	3.9	48.3	35.5
25	4.5	49.7	36.8
26	6.1	51.7	37.9
27	5.0	50.0	36.6
28	6.2	51.2	37.1
29	6.2	51.3	37.2
30	2.2	47.3	36.0
31	6.0	51.2	37.3
32	5.1	50.3	37.0
33	5.4	50.8	37.5
34	5.5	50.1	36.3
35	2.8	48.0	36.2
36	3.5	48.5	36.1
37	5.8	50.8	36.9
38	4.5	49.4	36.4
39	3.9	48.1	35.1
40	3.8	49.0	36.5



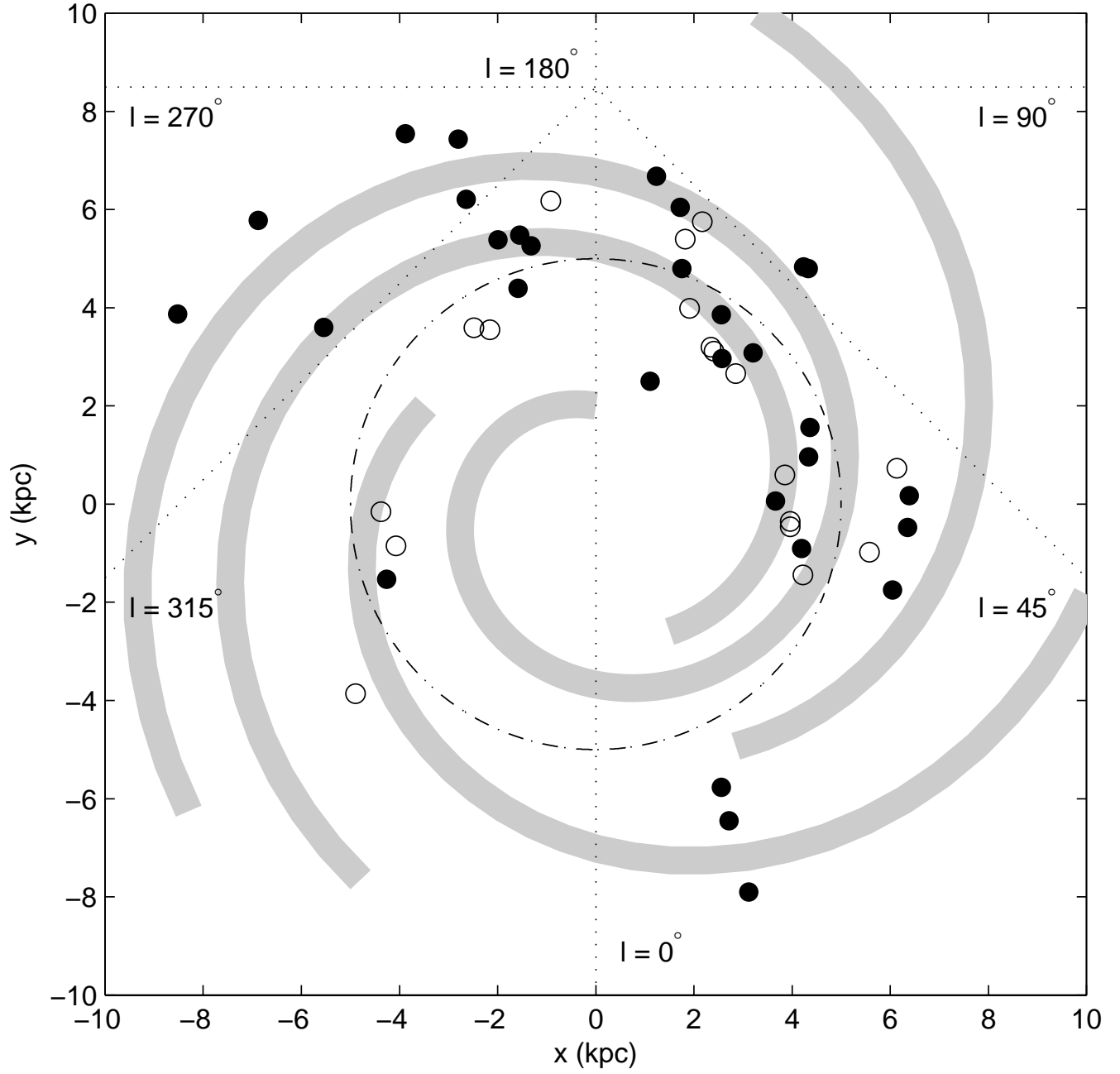


Figure 3. The Galactic distribution of the Star Forming Regions identified in this analysis. The filled circles indicate sources for which a unique distance has been determined, while open circles represent sources for which the kinematic distance is ambiguous remains. Both the near and far distances of these sources are presented. The spiral arms overlaid are taken from Nakanishi & Sofue (2006).

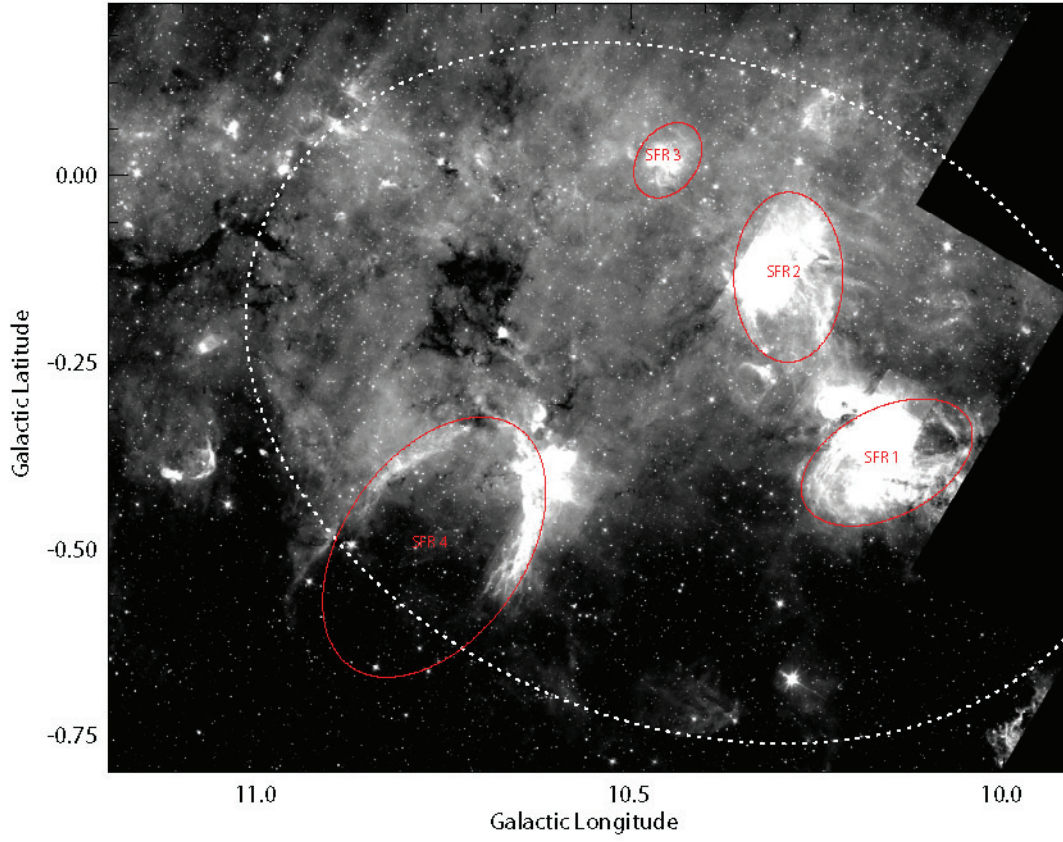


Figure 4. The 8μm GLIMPSE Image of the star forming regions in G10

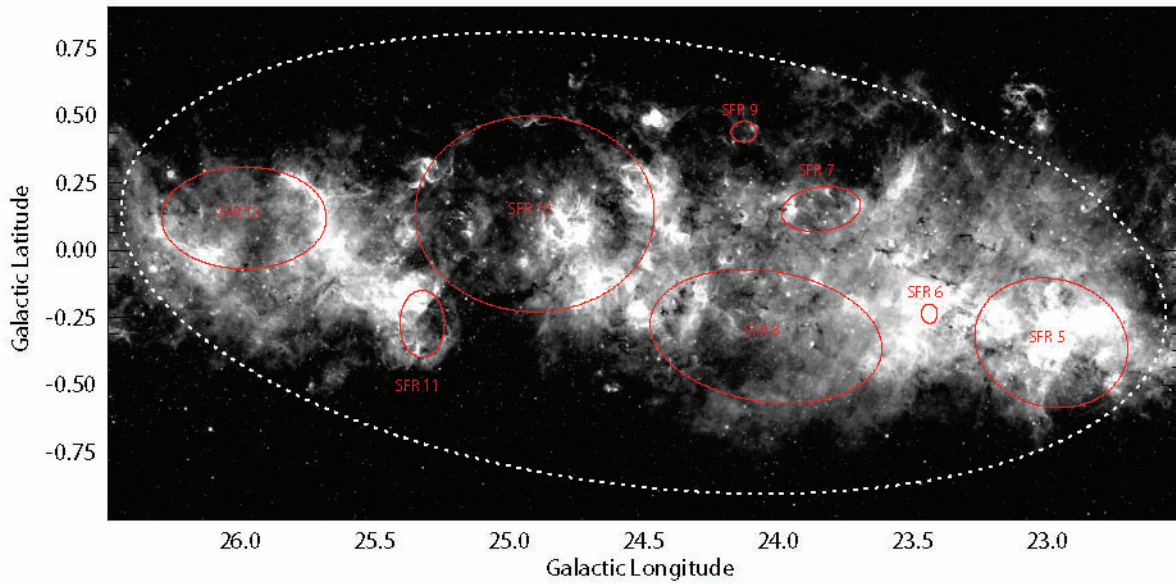


Figure 5. The 8μm GLIMPSE Image of the star forming regions in G24

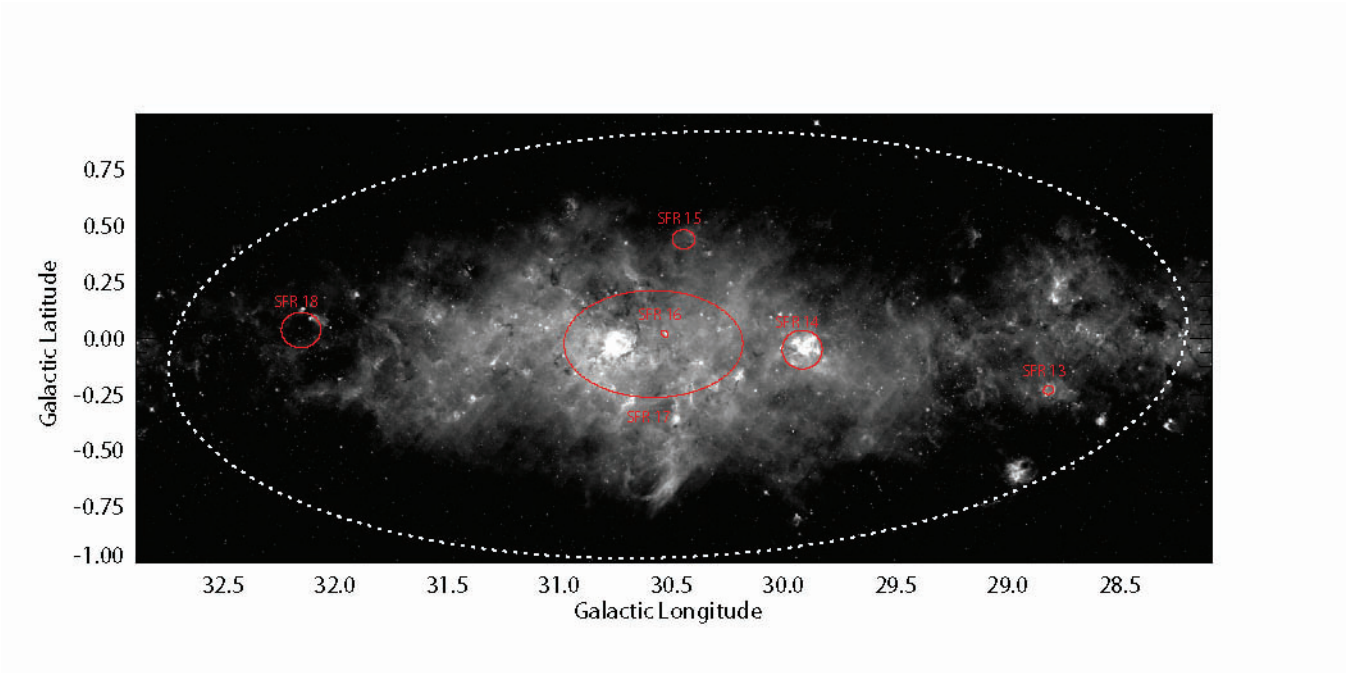


Figure 6. The 8μm GLIMPSE Image of the star forming regions in G30

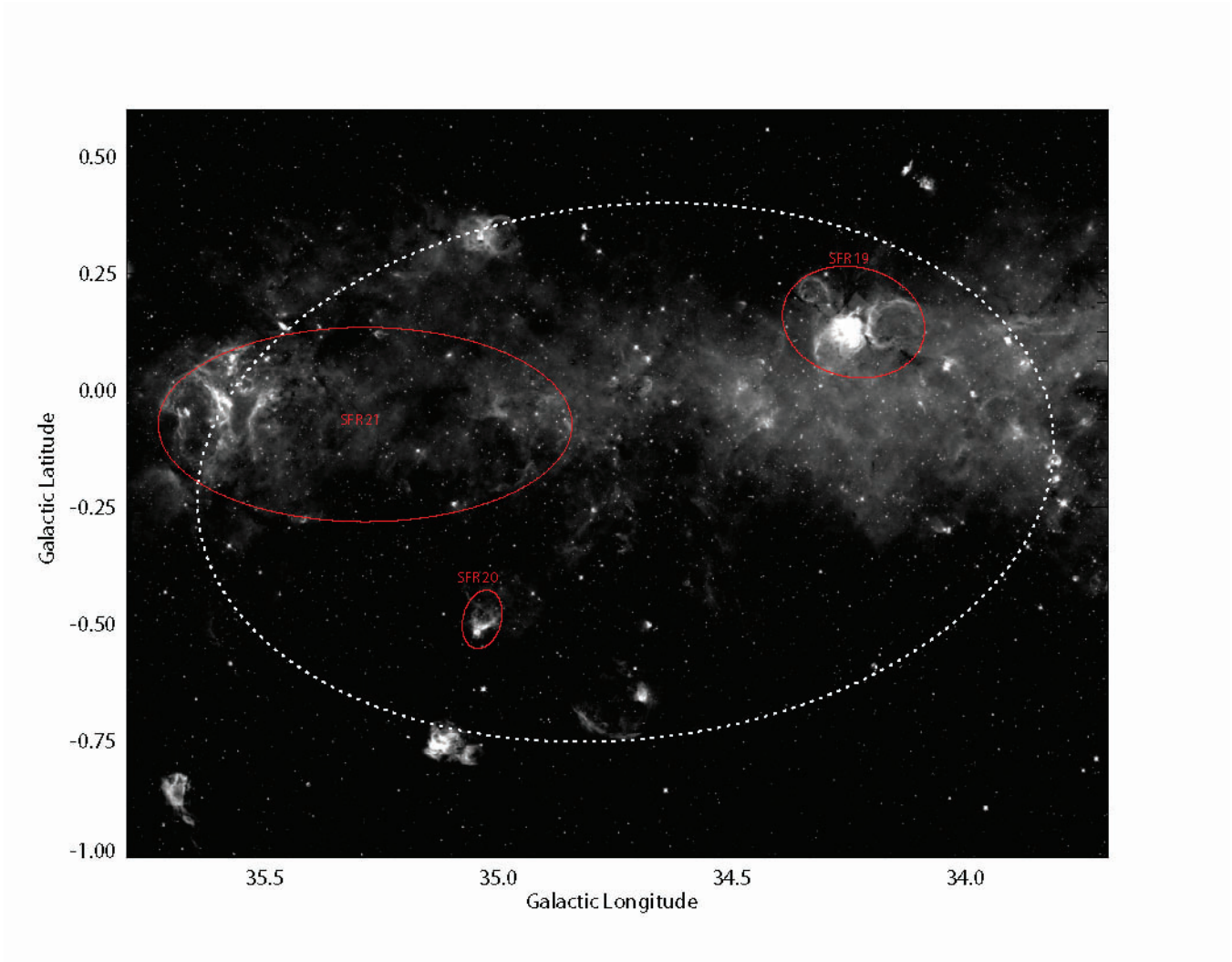


Figure 7. The 8μm GLIMPSE Image of the star forming regions in G34

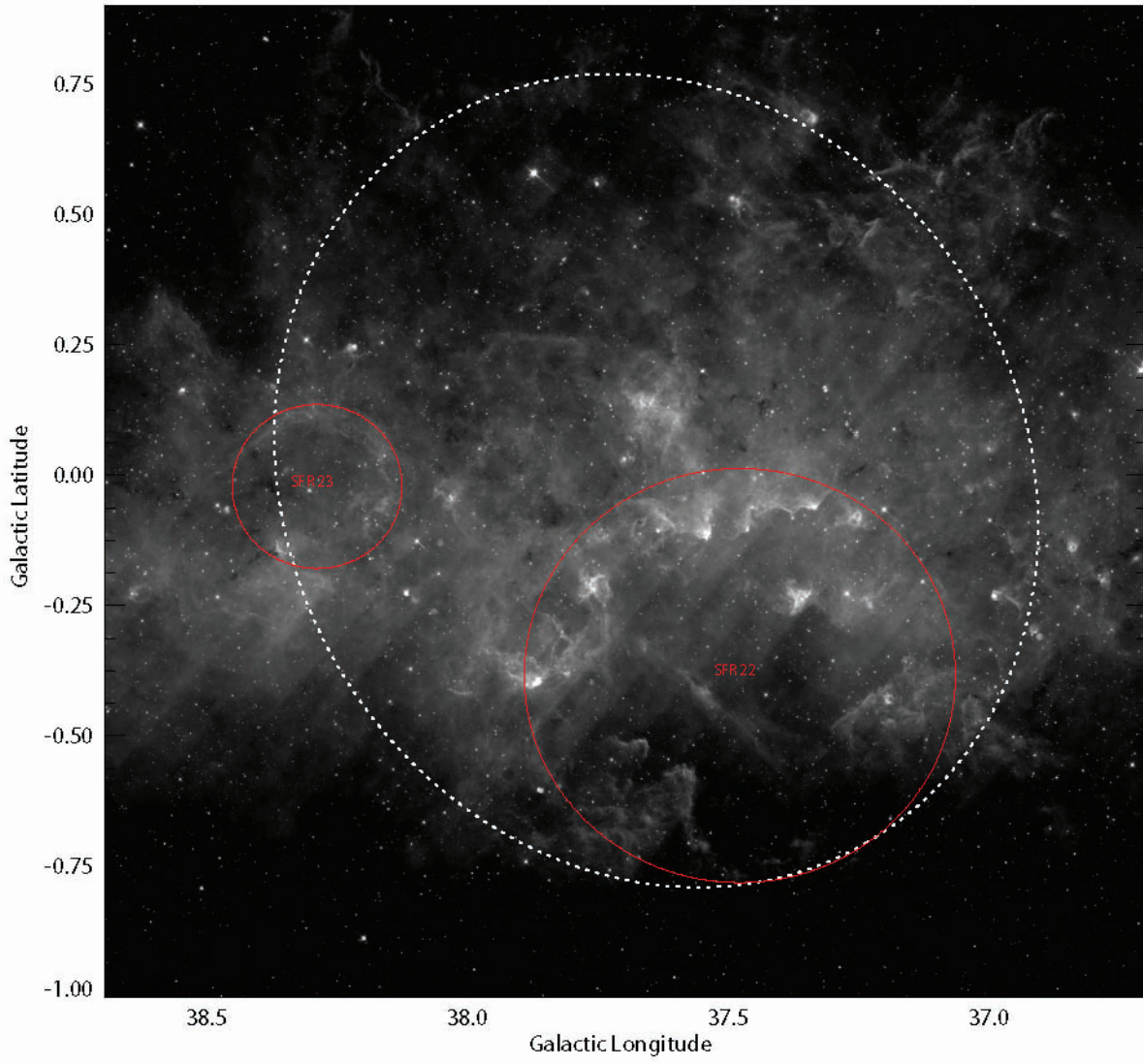


Figure 8. The 8μm GLIMPSE Image of the star forming regions in G37

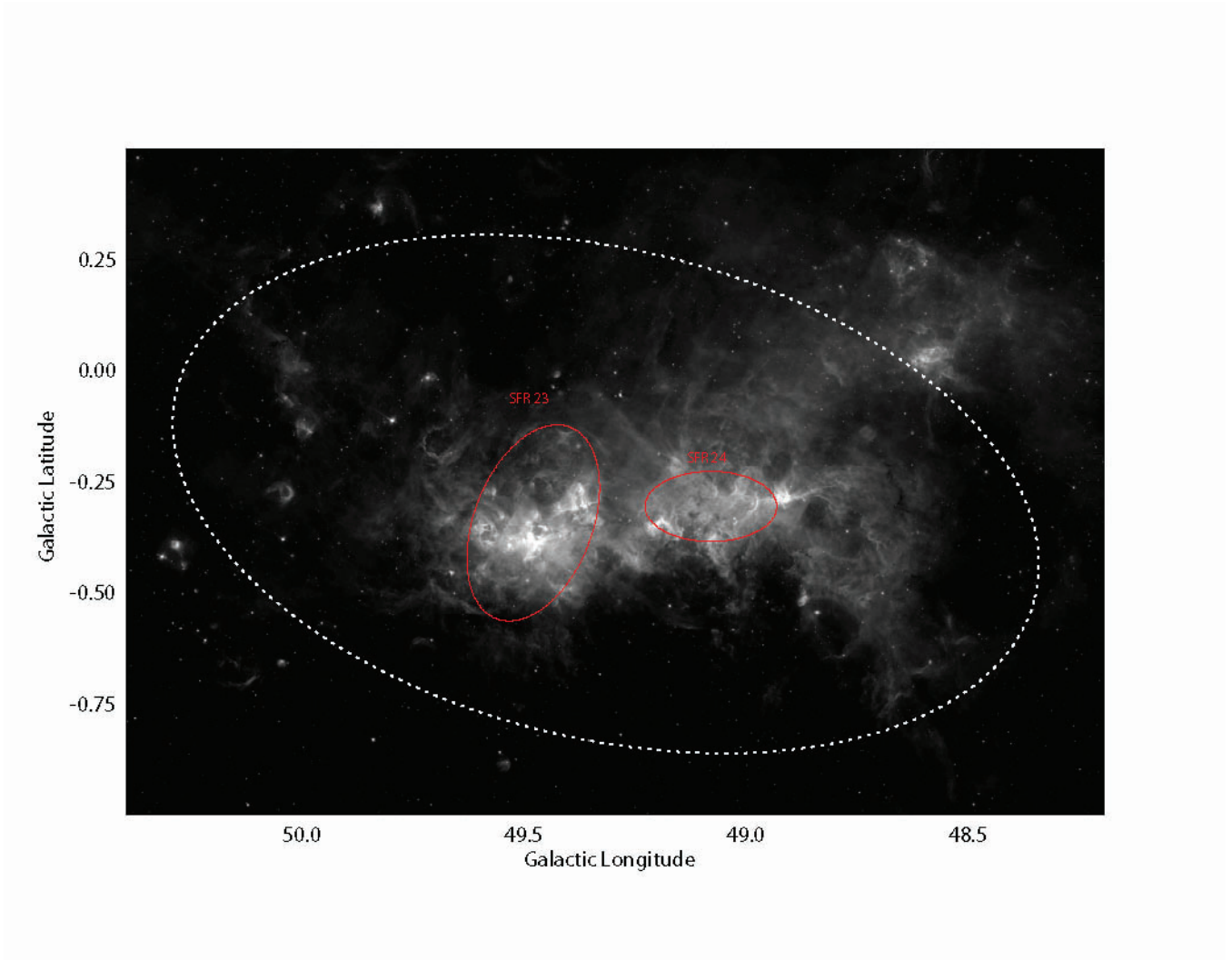


Figure 9. The 8 μ m GLIMPSE Image of the star forming regions in G49

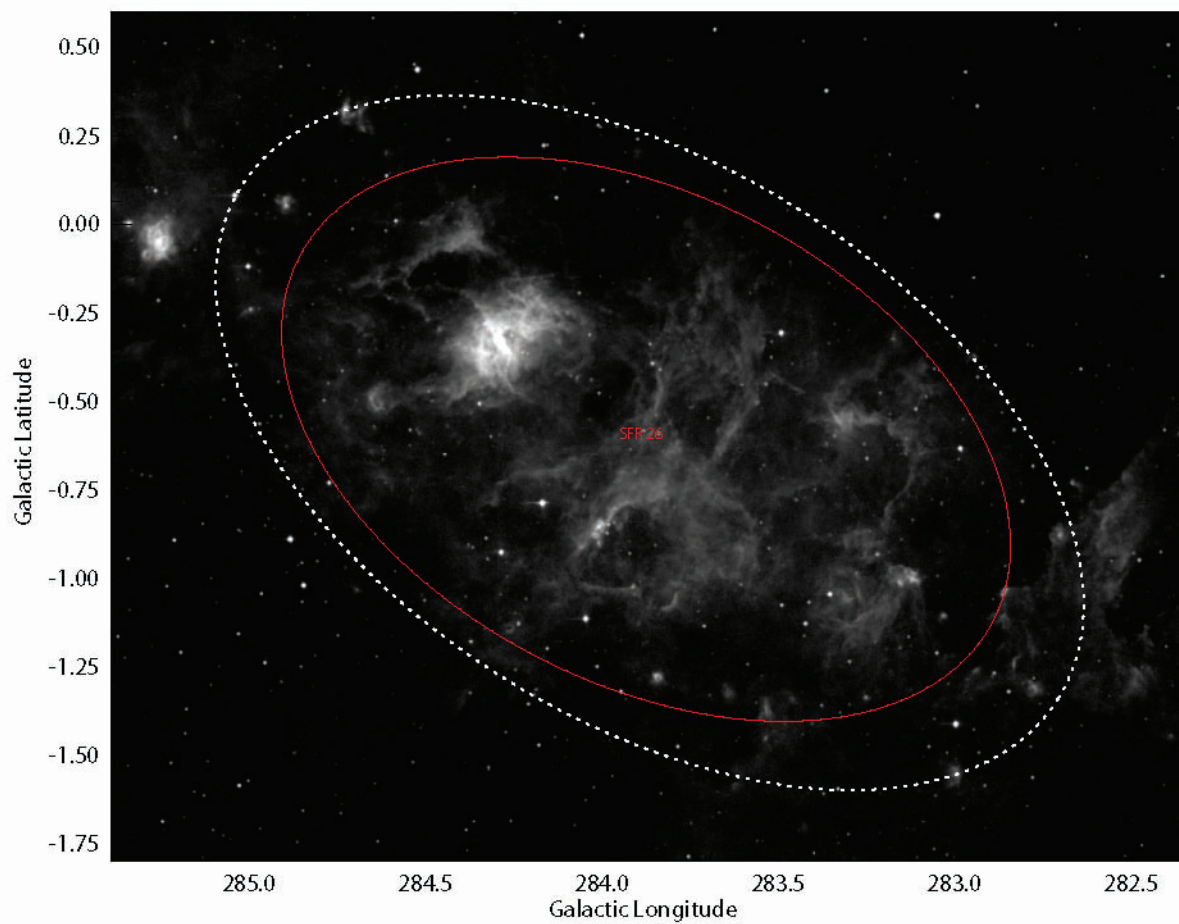


Figure 10. The 8μm MSX Image of the star forming regions in G283

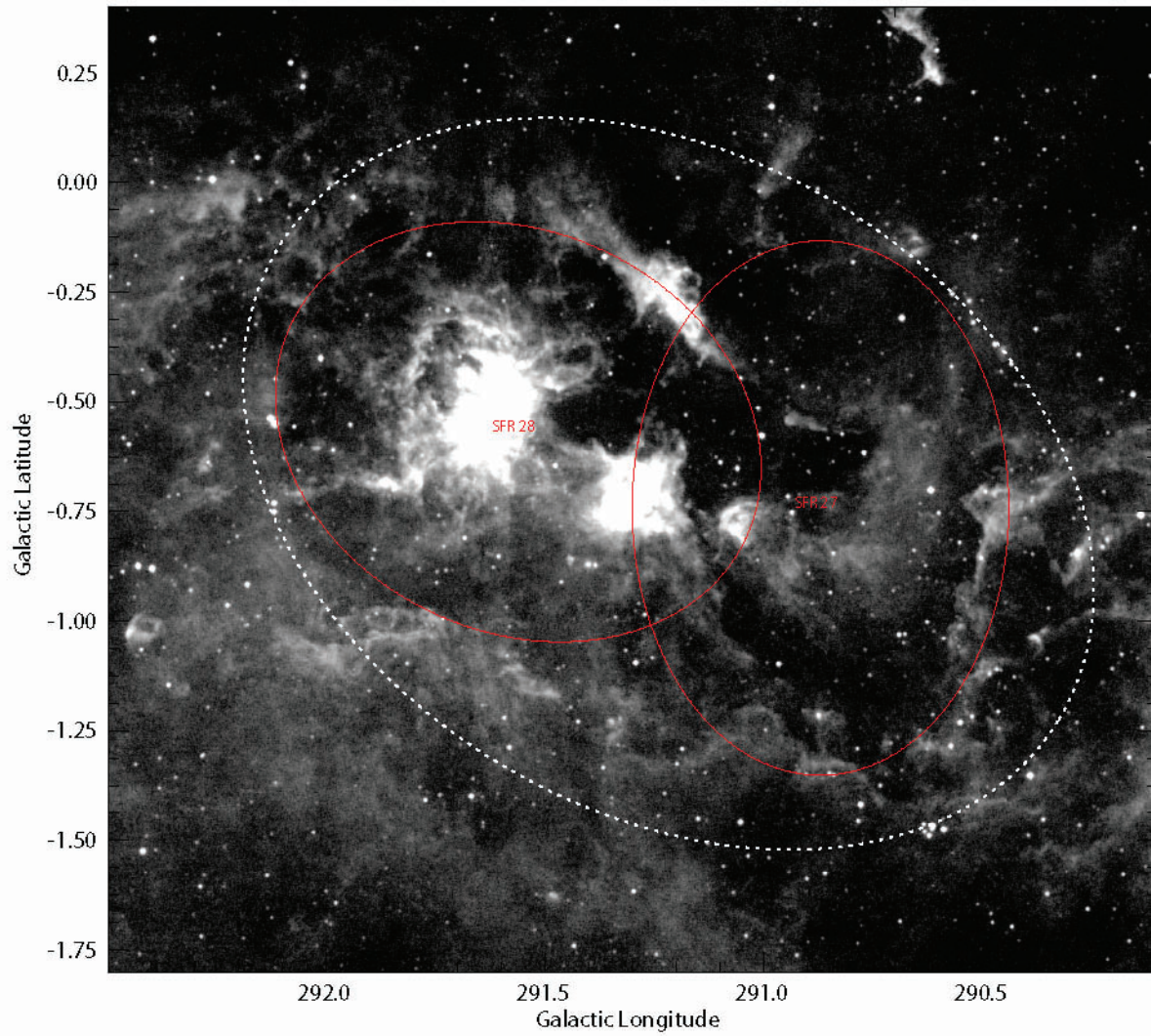


Figure 11. The 8μm MSX Image of the star forming regions in G291

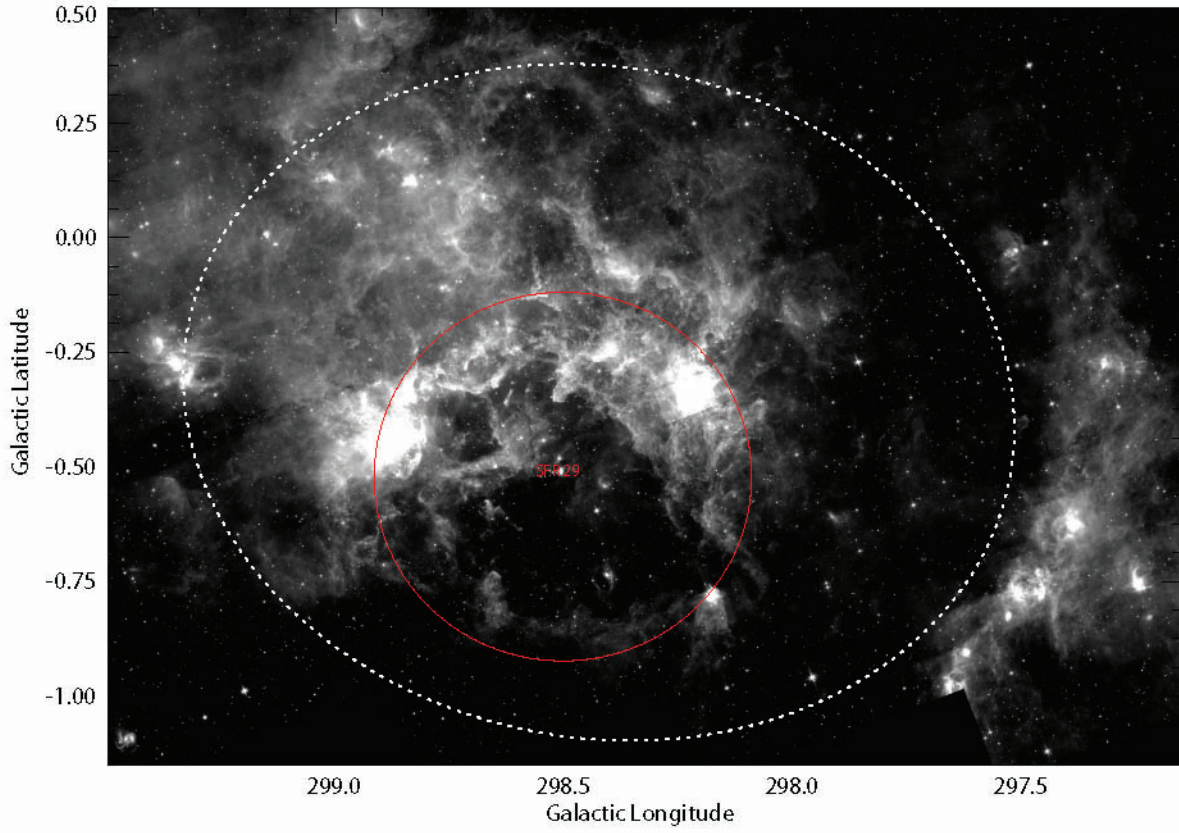


Figure 12. The 8 μ m GLIMPSE Image of the star forming regions in G298

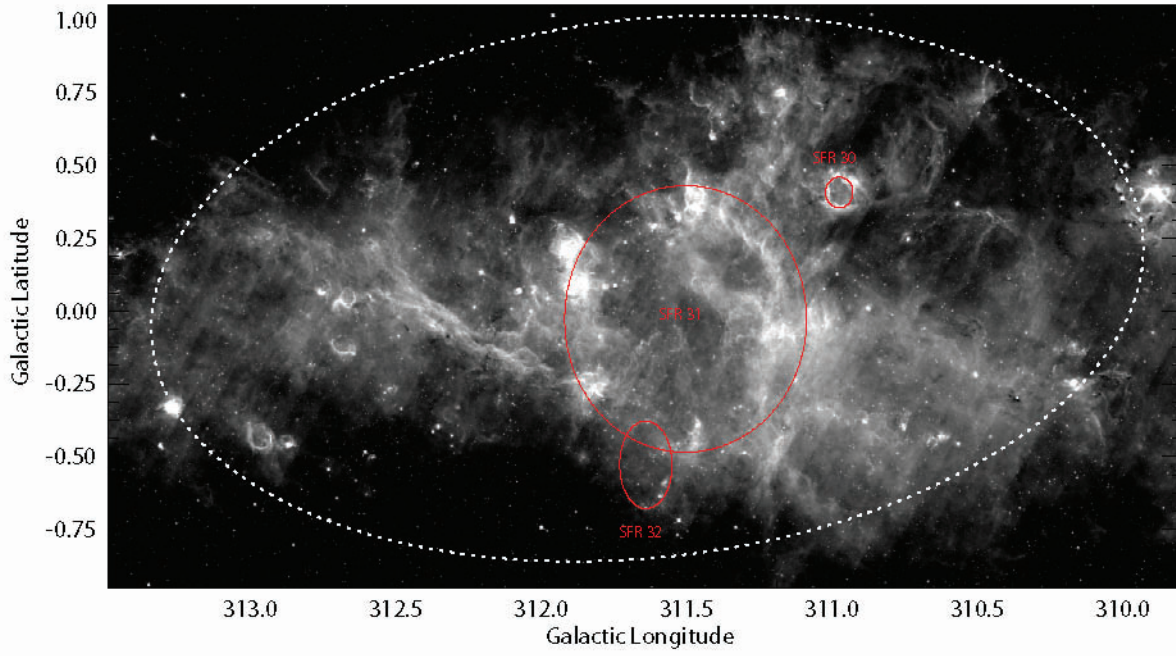


Figure 13. The 8μm GLIMPSE Image of the star forming regions in G311

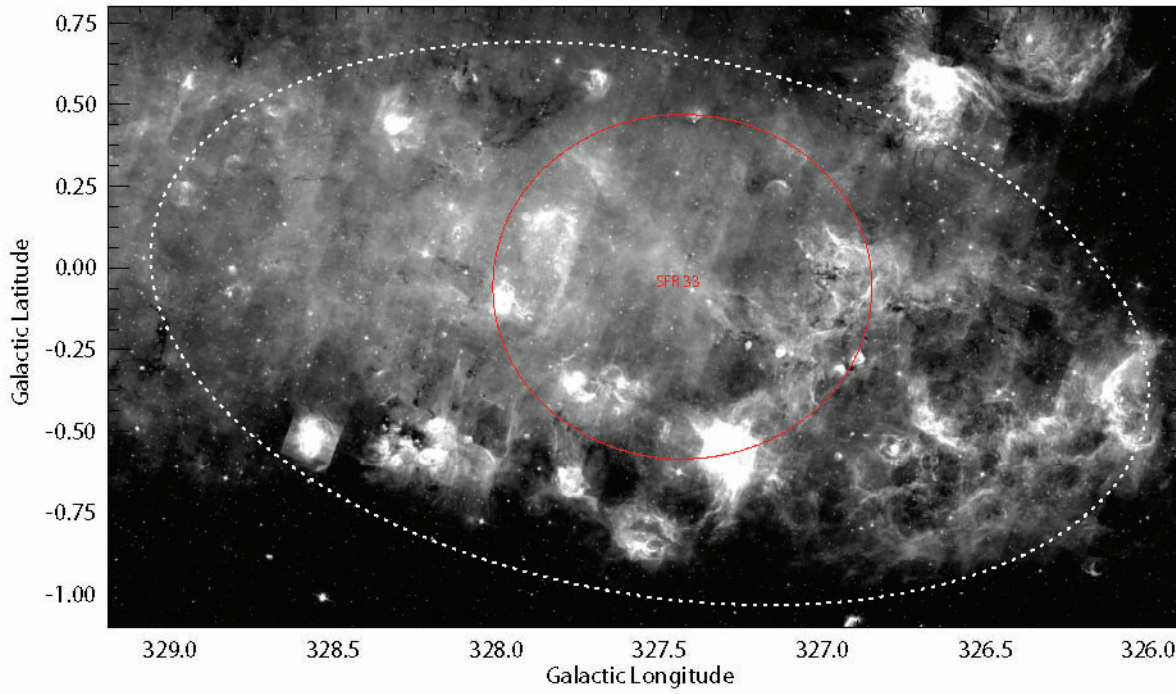


Figure 14. The 8μm GLIMPSE Image of the star forming regions in G327

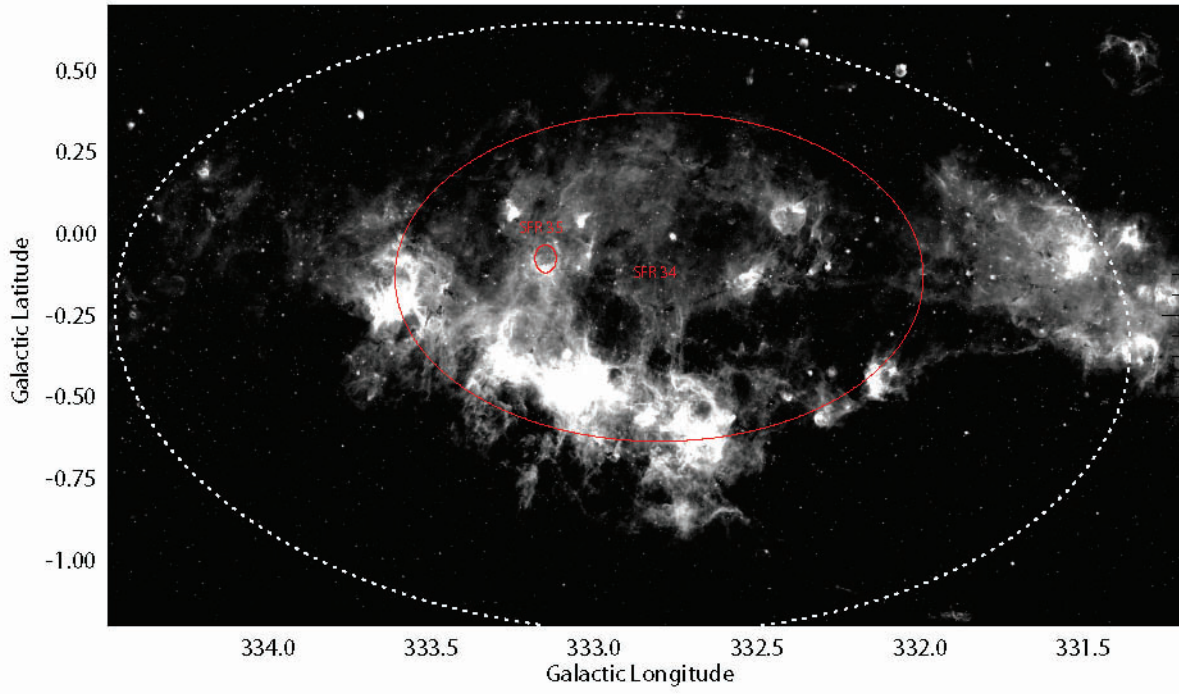


Figure 15. The 8μm GLIMPSE Image of the star forming regions in G332

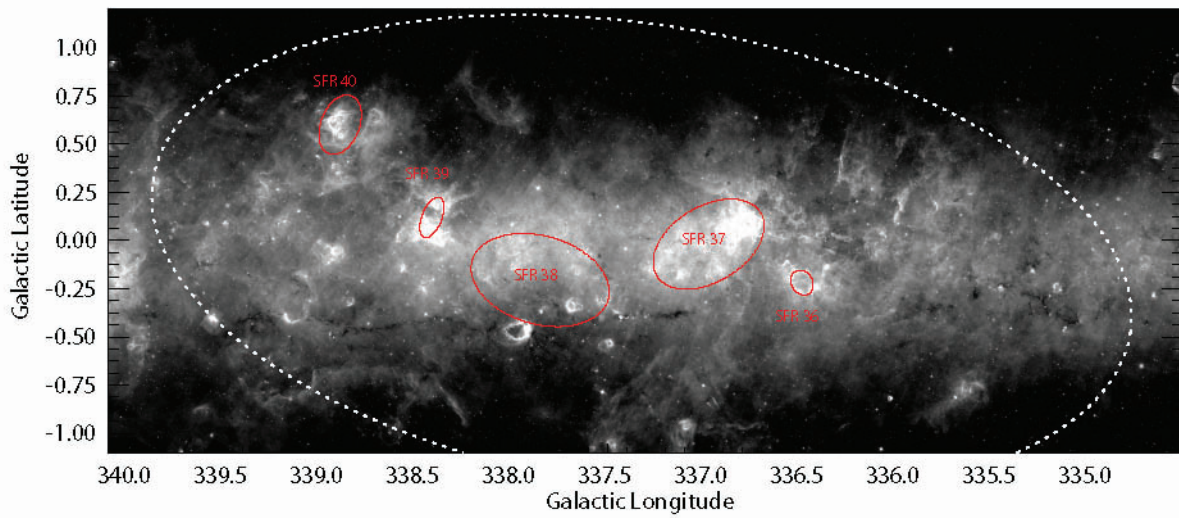


Figure 16. The 8μm GLIMPSE Image of the star forming regions in G337

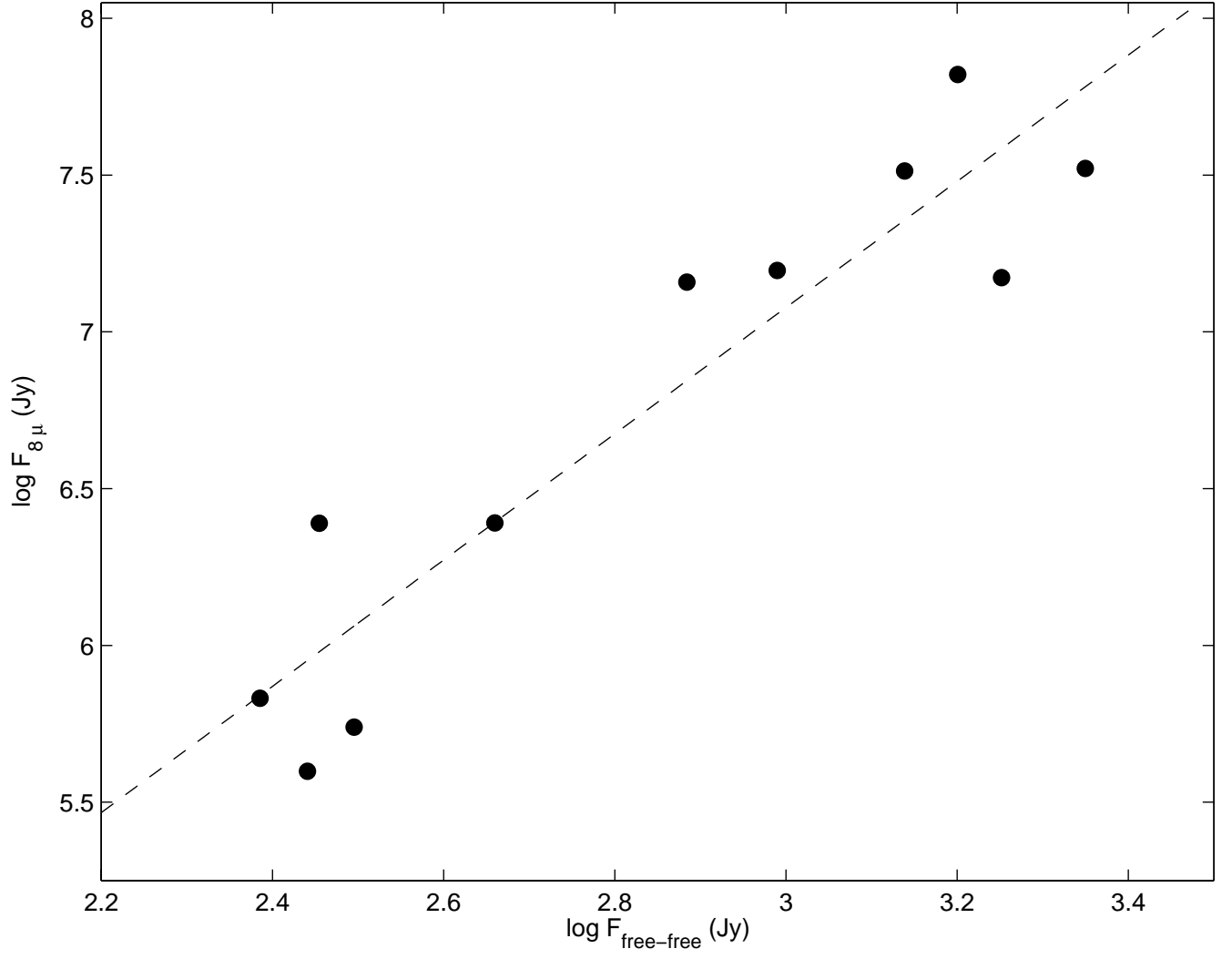


Figure 17. The comparison between the total flux integrated over the regions presented in Table 1 in free-free emission through the WMAP free-free foreground emission map at 90 GHz, and in PAH emission taken through the GLIMPSE 8 micron mosaics. The slope of the best fit line is 2.0 ± 0.3 . Regions without GLIMPSE coverage are excluded from this plot.